DEPARTMENT OF
MATERIALS SCIENCE

NOVA SCHOOL OF
SCIENCE & TECHNOLOGY

APOLO FILIPE DE RAMOS ESTRELA
Bachelor in Micro and Nanotechnology Engineering

FABRICATION AND CHARACTERIZATION OF CELLULOSE BASED CANTILEVERS FOR SENSING APPLICATIONS

MASTER IN MICRO AND NANOTECHNOLOGIES ENGINEERING

NOVA University Lisbon
September, 2023

DEPARTMENT OF
MATERIALS SCIENCE

FABRICATION AND CHARACTERIZATION OF CELLULOSE BASED CANTILEVERS FOR SENSING APPLICATIONS

APOLO FILIPE DE RAMOS ESTRELA

Bachelor in Micro and Nanotechnology Engineering

Adviser: Joana Maria Dória Vaz Pinto Morais Sarmento
Assistant Professor, SST NOVA

Co-adviser: Diana Filipa Pereira Gaspar
Senior Researcher, AlmaScience CoLab

Examination Committee

Chair: Hugo Manuel Brito Águas
Associate Professor, SST NOVA

Rapporteur: João Pedro de Sousa Oliveira
Assistant Professor, SST NOVA

Member: Joana Maria Dória Vaz Pinto Morais Sarmento
Assistant Professor, SST NOVA

MASTER IN MICRO AND NANOTECHNOLOGIES ENGINEERING

NOVA University Lisbon
September, 2023

Fabrication and characterization of cellulose based cantilevers for sensing applications

Acknowledgements

I write these words with a sense of profound happiness and satisfaction to signal a significant milestone within my professional trajectory. First and foremost, I would like to thank Professors Joana Pinto and Diana Gaspar for giving me the opportunity to work on this topic. I had the privilege of working with fantastic mentors who were always available to support me. I would also like to thank Professor Luís Pereira and his research group for giving me the opportunity to meet an incredible group of researchers who use this great environment to expand the horizons of science. I thank Professor João Canejo and researchers Mariana Matias, Tomás Freire, and Pedro Moreira for their kindness and their invaluable assistance.

Fortunately, I was able to carry out my work at CENIMAT, a renowned research center equipped with the latest technology in various areas of advanced material characterization and fabrication.

At this point, I would like to express my gratitude to FCT NOVA and to all the professors I had the privilege to meet during this educational journey. These were five years of experiences and learning that changed my perspective on science, technology, and above all, the world. FCT NOVA was the school where I grew and absorbed ethical and professional values and principles that I intend to carry into my professional practice.

My final thank you is for the people who have always been there. To my fellow classmates, Daniel, Tiago, Nuno, João, Luís, Catarina, and Maria. I thank you for your companionship and true friendship. Together, we experienced five years of hard work, overcoming challenges, and many moments of celebration and camaraderie. I am deeply grateful to my family, as they are the true architects of this thesis, always encouraging me to study and work hard. I thank my grandparents, aunts, uncles, and godparents. I thank my sister Diana, my father Luís, and my mother Margarida for being my great role models and my greatest inspirations. Thanks to these three people, to whom I owe who I am today and how I will think tomorrow.

I am thankful for sharing this journey with everyone.

"Doubt is not a pleasant condition, but certainty is absurd."

— Voltaire, Philosopher

Abstract

Electronic waste management is a global challenge. The solution lies in the technological renewal of devices and their materials. The field of sensors can contribute to this technological reform by focusing on the production of efficient, eco-friendly, and affordable sensors. This work aims to produce cantilevers on cellulose-based substrates for sensor applications.

Cantilevers are versatile structures easily integrated into various sensors. On the other hand, paper serves as a "green" substrate, well-known and implemented in diverse sensor systems, allowing the adoption of sustainable production methods based on simple, economical, and industrially reproducible systems.

This study delved into the geometry, optimized production through laser cutting, and determined the elastic constant of paper cantilevers with dimensions of 1 mm x 5 mm. Contact profilometry was employed to extract the mechanical properties of different substrates: i) printing paper with two grammages (80 $g.m^{-2}$, 120 $g.m^{-2}$); ii) printing paper coated with wax or nanofibrillated cellulose membrane; and iii) chromatographic paper. The cantilevers exhibited elastic constants, k_c, ranging from 1 to 3 $N.m^{-1}$, with varying variability between devices. The morphology, roughness, thickness, and elasticity of the substrates used were analyzed. Additionally, electrodes produced via Laser Induced Graphene (LIG), inkjet printing, and screen printing were tested, which could be used in deflection signal reading.

The outcome of this work was the production of model cantilevers. Optimized devices were achieved on commercial paper substrates of 80 $g.m^{-2}$ coated with cellulose membranes, measuring 2 mm x 5 mm, and exhibiting an average k_c of 5 $N.m^{-1}$. A silver read-out system printed via screen printing was also tested, displaying an average resistance of 260 Ω between electrodes.

This prototype validates and reaffirms the potential of cellulose-based cantilevers in the sensor field.

Keywords: Paper, cantilever, sensors, profilometry, NFC membrane, screen printing

Resumo

A gestão do lixo eletrónico é um desafio global. A solução passa pela renovação tecnológica dos dispositivos e seus materiais. A área sensorial pode participar nesta reforma tecnológica, privilegiando a produção de sensores eficientes, ecológicos e baratos. Este trabalho visa a produção de cantilevers em substratos celulósicos para aplicações sensoriais.

O cantilever é uma estrutura versátil e facilmente integrável em vários sensores. Por outro lado, o papel constitui um substrato "verde", já conhecido e implementado em diversos sistemas sensoriais, permitindo a adoção de métodos de produção sustentáveis que têm por base sistemas simples, económicos e reproduzíveis à escala industrial.

Neste trabalho estudou-se a geometria, otimizou-se a produção por corte a laser e determinou-se a constante elástica de cantilevers de papel com dimensões de 1 mm x 5 mm. Foi utilizada a técnica de perfilometria de contacto para se extrair as propriedades mecânicas de diferentes substratos: i) papel de impressão com duas gramagens (80 $g.m^{-2}$, 120 $g.m^{-2}$); ii) papel de impressão revestido com cera ou membrana celulósica nanofibrilada e iii) papel cromatográfico. Os cantilevers apresentam constante elástica, k_c, entre 1 e 3 N/m, com diferente variabilidade entre dispositivos. Analisou-se a morfologia, rugosidade, espessura e a elasticidade dos substratos utilizados e ainda foram testados elétrodos, produzidos por LIG (*Laser Induced Graphene*), *inkjet printing* e *screen printing* que poderão ser usados na leitura do sinal de deflexão.

O trabalho resultou na produção de cantilevers modelo. Os dispositivos otimizados foram obtidos em substrato de papel comercial 80 $g.m^{-2}$ revestidos por membranas celulósicas, com dimensões de 2 mm x 5 mm e apresentando um k_c médio de 5 $N.m^{-1}$. Foi testado ainda um sistema read-out de prata impresso por screen-printing com uma resistência média de 260 Ω entre elétrodos.

Este protótipo valida e reafirma o potencial dos cantilevers celulósicos na área sensorial.

Palavras-chave: Papel, cantilever, sensores, perfilometria, membrana de CNF, screen-printing

Contents

List of Figures

List of Tables

Acronyms

CMN120 Nanofibrillated cellulose membrane over Navigator paper 120g.m^{-2} substrate
CMN80 Nanofibrillated cellulose membrane over Navigator paper 80g.m^{-2} substrate
CP Whatman chromatography paper grade 1 substrate

ePOC Proof of concept with printed electrodes cantilever

FRCP Fire retardant treated Whatman chromatography paper grade 1 substrate
FRN80 Fire retardant treated Navigator paper 80 g.m^{-2} substrate

LIG Laser Induced Graphene

N120 Navigator paper 120 g.m^{-2} substrate
N80 Navigator paper 80 g.m^{-2} substrate
NFC Nanofibrillated Cellulose

P-C Parylene-C substrate
PEN Poly(ethylene 2,6-naphthalate) substrate
POC Proof of concept cantilever

RN80 90ºC rotated Navigator paper 80 g.m^{-2} substrate

SEM Scanning Electron Microscopy

WN120 Wax coating over Navigator paper 120 g.m^{-2} substrate
WN80 Wax coating over Navigator paper 80 g.m^{-2} substrate

Symbols

A	Cross-sectional area
Δl	Difference between the final and the initial length of the sample
Δz	Deflection of the cantilevers on the Z-axis
E	Young's modulus
F	Force
$\mathbf{k}_c$	Cantilever elastic constant
L	Length
$\mathbf{l}_0$	Initial length of the sample
v	Poisson ratio
R	Resistance
r	Roughness
RPM	Rotations per minute
$\mathbf{s}_t$	Strain
σ_s	Stress
t	Thickness
W	Width

1

Context and Objectives

Currently, society relies on technology like never before. In January 2023, out of the world's 8.01 billion population, it is estimated that 68% of the global population owns a mobile phone, with 64% using it worldwide and spending an average of 6 hours and 37 minutes per day on it [49]. In this increasingly connected world, technological advancement has been the primary driver of electronic waste (e-waste) production [1, 2].

In 2015, the United Nations established a set of 17 objectives aimed at the social and economic development of countries and their populations [3]. Goal 12, "Responsible Consumption and Production," is one of the most comprehensive because it is not limited to a specific industry or area [4, 5]. This objective is of particular importance as it aims to address global challenges such as responsible management of terrestrial resources and the production and proper treatment of waste. The work associated with this goal involves reevaluating consumerist social habits, production strategies, and materials used [6].

The present work aims precisely to address these problems by exploring new raw materials and production methods that ultimately reduce or facilitate the recycling of electronic waste. The field of sensory technology is of significant social interest, and the production of efficient, eco-friendly, and cost-effective sensory systems should be a common goal within the scientific community.

In this context, this work aims to produce and characterize cantilevers on cellulose-based substrates for sensory applications. Specifically, this project focuses on optimizing the device geometry, manufacturing using simple and cost-effective techniques such as laser cutting, and mechanically characterizing the structures to assess the validity of these sensors. Once the cantilevers' sensitivity is determined, the implementation of a transduction system from mechanical to electrical signals will be studied.

Additionally, to gain a better understanding of the designed system, mechanical and morphological characterization of the target substrates will be conducted in parallel.

2

Concepts and State of the Art

2.1 Paper and Cellulose-Based Substrates

Paper, a readily available and cost-effective material, has gained significant attention in several fields of science and engineering. The unique properties of paper, such as its flexibility, high surface area, and porosity, make it an ideal candidate for sensing applications. Paper serves as both a structural support and a sensing element, enabling the detection of various analytes or stimuli [7]. Moreover, paper can be easily modified or functionalized to enhance its sensing capabilities, opening up new possibilities for customization and sensor development [8].

2.1.1 Paper's Chemical Properties

Starting with wood, the cell walls of plant cells are composed of cellulose, hemicellulose, lignin, and other organic and inorganic extracts. Therefore, the chemical composition of a sheet of paper depends on the raw material (cotton, bamboo, linen) and the chemical methods used to produce the paper pulp. Wood is the most used raw material due to its abundance and low cost [9].

Several studies confirm that cellulose is the most abundant element in the final composition of paper pulp and, therefore, in paper [9]. Cellulose is a naturally occurring polysaccharide, made up of linear, homogeneous glucose (1,4-D-glucopyranose) monomers with a degree of polymerization ranging from 3000 to 15000 [8]. The natural type of cellulose found in nature, cellulose I, is one polymorphism of cellulose that differs in terms of their crystallinity and stability [10]. Due to its high degree of polymerization and crystallinity, cellulose I generates exceptionally strong fibers that are linked by hydrogen bonds between the hydroxyl groups in glucose monomers and is responsible for structural activities within the cell wall of plant cells.

The hemicellulose is the second most prevalent component in wood. Low molecular weight heterogeneous polysaccharides make up hemicelluloses [9]. Cellulose and hemicellulose are unrelated since their synthesis occur via separate processes. As a result, hemicelluloses in vegetable cell walls lack any structural characteristics. On paper, though, they offer useful qualities. The connection between crystalline cellulose and amorphous lignin is caused by hemicelluloses, which surround cellulose microfibrils using Van der Walls forces and hydrogen bonds [11].

Commercial printing paper, the main substrate used in this work, is a substrate composed of a dense network of cellulose fibers, filler particles (usually kaolin, calcium carbonate, or other mineral components), and air. In some cases, a thin layer of mineral pigments is deposited on the surface of the paper to improve the printability of the papers or to give a specific color (usually kaolin, calcium carbonate, other minerals, or a mixture of these pigments) [12, 13].

2.1.2 Paper's Physical Properties

From a structural perspective, crystalline cellulose of an elementary fibril has a tensile strength between 7.5 and 7.7 GPa and a Young's modulus ranging from 110 to 220 GPa [14–16]. With a tensile strength ranging from 0.3 to 1.4 GPa and a Young's modulus spanning from 14 to 27 GPa, micro-sized cellulose fibers self-assembled by helically oriented elementary fibrils have noticeably lower mechanical properties [17]. On the other hand, bulk wood made of microscale cellulose fibers exhibits a tensile strength ranging from 50 to 140 MPa and a modulus ranging from 2 to 14 GP. These properties indicate a significant decrease in mechanical strength during the biosynthesis process [18]. In paper, we predominantly find a mixture composed of cellulose. Therefore, it is expected that the mechanical properties of paper would approach the behavior of cellulose fibers at the microscale from 2 to 14 GPa.

Furthermore, the amount of hemicellulose in paper also affects its tensile-resistant behaviour [19]. Tensile strength reportedly rises with higher dosages of such carbohydrates [20, 21] . Hemicelluloses provide significant contributions to intra and interlinked fiber, giving handsheets more tensile resistance.

2.2 Cantilever Physical Principle and Mathematical Considerations

In general, there are two main modes of transduction and recognition of an event or analyte that can lead to the micro-mechanical response of the cantilever [22, 23]:

1. Change in oscillation frequency due to an applied force;
2. Change in the deflection due to an applied force.

This work was developed based on the latter operating principle, and therefore, the following are the most relevant considerations for this transduction method.

As described earlier, the functioning principle of the cantilever is based on its bending when a force is applied to its end. This relationship can be described through

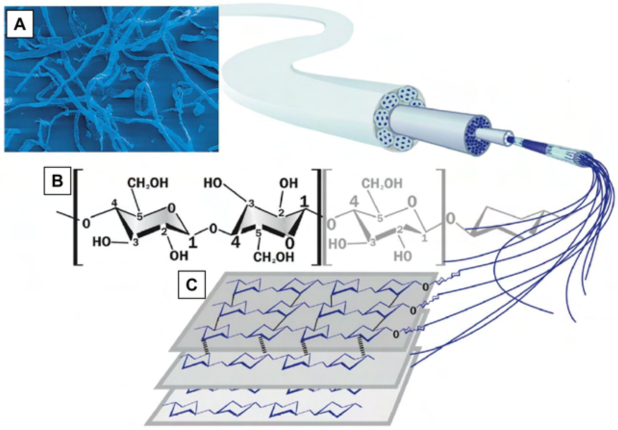

Figure 2.1: Chemical and macroscopic structure of cellulose. Cellulose is a biopolymer distributed in fibers (**A**), consisting of linear chains of glucose monomers (**B**). These chains interconnect through hydrogen bonds, forming fibrils, which collectively create a cellulose fiber (**C**). Adapted from [50].

Hooke's law (equation 2.1), where the deflection of the structure is directly proportional to the applied force (F) and, again, directly proportional to the cantilever's elastic constant (k_c). It is the cantilever's elastic constant that determines the system's properties, such as flexibility or the final sensitivity of the sensor [24].

$$F = -k_c \Delta z \tag{2.1}$$

On the other hand, the cantilever's' elastic constant is a multi-factorial quantity that depends on the cantilever's width and length (W, L), substrate's thickness t, and the Young's modulus (E) of the material constituting the cantilever.

$$k_c = \frac{Et^3 w}{4l^3} \tag{2.2}$$

The complete derivation of the presented expressions, as well as the comparison with tensile tests, can be found in annex II.1.

The first approach in this work involved working backward from the description above, i.e., defining the material, cantilever dimensions, studying the deflections experienced when different forces were applied, and attempting to obtain the value of substrate's elasticity (equation 2.2) by comparing it with theory. Only in this manner can we ensure the reliability of k_c results and characterize the produced cantilevers with a high degree of confidence.

As we are working with a cellulose-based and porous substrate, atmospheric relative humidity is a factor that may impact the natural deflection of the device. It is important to note that to reduce this impact, most of the work was conducted during the summer when very low relative humidity values were recorded. Another important aspect, in contrast to the negligible humidity, is the influence of surface stress when the cantilever has a thinner film on its surface, affecting the deflection of the structure (Δz). There are still many points of contention on this topic; however, the most consensus formula that seeks to explain this relationship is Stoney's formula (equation 2.3) [22] .

$$\Delta\sigma = \frac{Et^2}{3(1-v)L^2}\Delta z \tag{2.3}$$

In this formula, v represents the Poisson ratio and $\Delta\sigma$ represents the surface stress. Again, the surface tension depends on the geometry (L,W), the thickness and the elasticity of the cantilever substrate. As per theory [25], wood pulp paper displays a Poisson's ratio of 0.169.

2.3 Deflection via Contact Profilometry

A profilometer is an instrument typically used in metrology. In this analysis technique, the constant force scanning of the tip on the sample's surface reveals its morphological properties and allows us to determine characteristics related to variations in height, such as marking the height of certain layers or the depth of pores in a particular substrate.

There was already some work developed in this new direction [26, 27]; however, it was only in 2006, He and his team demonstrated that this equipment can also be used to mechanically characterize cantilevers by continuously scanning the tip over the cantilever and measuring its deflection [28]. By repeating this procedure for various forces, we can obtain deflection curves for different loads and thereby derive values for cantilever's elastic constant and substrate's elasticity, as demonstrated earlier [29].

Moreover, by moving the tip very slowly over the surface of the cantilever, we can assume that the equipment is recording deflections at nearly static points. This allows us to eliminate parasitic oscillation frequencies that could interfere with the ongoing deflection measurement.

In addition to deflection data, profilometry also provides us with information about the surface morphology of the cantilevers. All surface irregularities that the tip encounters are observable in the deflection curves.

However, this technique has some limitations related to cantilever anchoring. According to mathematical models, applying a constant force at one point on the cantilever assumes that the cantilever's anchoring is fixed, which is impossible to verify in the setup used and described further below (section 3.1). Also as discussed before, uncertainties associated with measurements of width, length, and thickness of the structure can easily deviate from reality, as well as the chosen location for scanning along the cantilever, resulting in natural variations in the final results [29].

2.4 Paper-Based Milicantilevers

Microcantilevers, with their exceptional sensitivity and versatility, have revolutionized the field of sensing and detection. These miniature structures, typically consisting of a thin beam anchored at one end, exhibit mechanical deflections in response to various external stimuli, such as mass deposition, surface stress, and temperature changes. The ability to convert these mechanical deflections into measurable signals has led to the development of a wide range of sensing applications, including chemical and biological detection, gas sensing, and environmental monitoring [30, 31].

Traditionally, microcantilevers have been fabricated using silicon-based materials and advanced microfabrication techniques, such as surface micromachining procedures (chemical etching, thermal oxidation, among others). However, in recent years, there has been growing interest in exploring alternative materials and fabrication methods to overcome the limitations associated with silicon-based devices. One such alternative is the use of polymeric substrates for millicantilevers, such as paper, offering several advantages, including low cost, ease of fabrication, and compatibility with mass production techniques [32].

2.4.1 Paper-Based Cantilevers' Properties

Paper-based microcantilevers present numerous advantages over traditional silicon-based devices. First and foremost, the low cost of paper makes it an attractive option for large-scale production and disposable applications [8]. This affordability is especially valuable in resource-limited settings, where cost-effective sensing solutions are essential [7].

Secondly, the flexibility of paper allows for the integration of microcantilevers into complex and non-planar surfaces. This feature enables the development of conformable sensors that can be easily adapted to various substrates, such as fabrics, plastics, and even human skin. The ability to create flexible and wearable sensors expands the potential applications of microcantilevers, ranging from healthcare monitoring to smart textiles (figure 2.2.A) [33, 34].

Furthermore, the porosity of paper provides an inherent advantage for gas and vapor sensing applications. The porous structure allows for efficient gas diffusion and enhances the sensitivity of the milli-cantilever-based sensors [35]. Additionally, the high surface area-to-volume ratio of paper facilitates the adsorption of target analytes, resulting in improved detection limits and response times [36].

2.4.2 Paper-Based Cantilevers' Applications

Paper-based microcantilevers have found applications in diverse fields, including environmental monitoring, healthcare and food safety. These sensors can detect a wide range of analytes, such as volatile organic compounds, heavy metals, biological molecules, and pathogens [37].

In environmental monitoring, paper-based milli-cantilevers have been employed for the detection of air pollutants, water contaminants, and hazardous gases (figure 2.2.B) [38, 39]. Their portability, ease of use, and real-time monitoring capabilities make them valuable tools for ensuring air and water quality in both indoor and outdoor environments.

In the healthcare sector, paper-based milli-cantilevers have shown promise in the detection of biomarkers for disease diagnosis and monitoring. By functionalizing the cantilever surface with specific receptors or antibodies, these sensors can selectively capture and detect target molecules, enabling early detection of diseases such as cancer, diabetes, and infectious diseases [37, 40].

Food safety is another critical area where paper-based milli-cantilevers can make a significant impact. They can be used to detect foodborne pathogens, toxins, and contaminants, helping to ensure the safety and quality of food products. The simplicity and low cost of these sensors make them particularly suitable for on-site testing in the food industry [38].

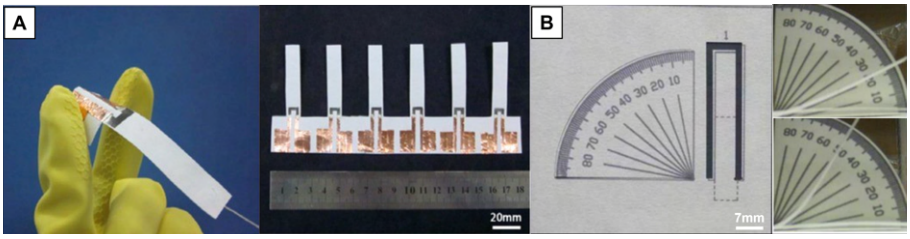

Figure 2.2: Milli-cantilever application examples. (**A**) Graphite-on-paper piezoresistive sensor, adapted from [41]. consisting of linear chains of glucose monomers. (**B**) Paper-based cantilever array sensor for organic compound monitoring, adapted from [38].

2.5 Tensile Test Overview

According to classical theory [42], the elasticity of materials can be determined through a tensile test. The raw data obtained from the equipment consists of force plotted against sample extension. The force applied during the test allows us to calculate the applied stress (σ_s) using the formula 2.4, where A represents the cross-sectional area. Furthermore, the sample's extension, Δl, is related to its geometry through the formula 2.5, where l_0 is the initial length of the sample before the test begins.

$$\sigma_s = \frac{F}{A} \tag{2.4}$$

$$s_t = \frac{\Delta l}{l_0} \tag{2.5}$$

The Young's modulus will be determined by calculating the slope of the linear regression line on the stress versus strain (s_t) graph.

There aren't many studies that perform a comparison between the Young's modulus obtained through tensile tests and the deflection of a material when subjected to an applied force. Some theories regarding the relationship between flexural and tensile tests for non-cellulosic materials exist [43, 44]. Therefore, in order to validate the results, it is important to establish a relationship between the two methods for determining elasticity and experimentally confirm the constancy of this relationship.

3

Materials and Methods

The descriptions related to the paper used, coating techniques, photographic record can be found in the annex section II.6. During the experimental activities, the average temperature and humidity recorded were 25.23 °C and 31%, respectively.

3.1 Cantilever Fabrication

During this project a reference Poly(ethylene 2,6-naphthalate) substrate (PEN) and three different paper substrates were used to fabricate the cantilevers: Navigator paper 80 $g.m^{-2}$ substrate (N80), Navigator paper 120 $g.m^{-2}$ substrate (N120), Whatman chromatography paper grade 1 substrate (CP). The specifications regarding the cellulose substrates used are provided in the annex II.2.

Two distinct coatings were applied to Navigator papers in an effort to reduce the material's roughness, namely nanofibrillated cellulose membrane and inkjet printed wax. The nanofibrillated membranes were prepared by blending 11.5 g of nanofibrillated gel with 2% solid content into 35 mL of deionized water, stirred for 15 min at 200 RPM. The resulting mixture was poured into a petri dish and placed in a desiccator for 15 h at 40 °C. Paper substrates (N80 or N120) were then added to this jellified suspension and then placed back in the desiccator for another 15 h at 40 °C. This method was adapted from previous works [45, 46], further details can be found in annex II.3. The wax coating was applied using a Xerox ColorQube 8570 inkjet printer.

The cantilevers were all cut using a VLS 3.5 laser cutting machine from Universal Laser Systems. Adobe Illustrator was utilized to design the cantilever shape and geometry. Various sizes were designed, ranging from lengths of 2 to 5 mm and widths of 0.5 and 1 mm. The power and velocity were optimized for each substrates as will be referred in section 4.2. The cantilevers were cut in groups of five, each having the same dimensions. This arrangement ensured that each substrate contained a set of similar cantilevers for testing purposes. A mark located 1 mm away from the fixed end of the cantilevers was engraved on the substrate, serving as a reference line. These substrates were then glued to an acrylic base using double side tape as can be seen in annex II.6.

3.2 Surface Characterization of Paper Substrates and Cantilevers

Optical characterization of the cantilevers was performed using an Optical Stereo Microscope Leica M80 from Leica Microsystems and SEM images were obtained from a tabletop TM3030 Plus Hitachi system with 200x magnification. 3D surface maps was performed on a XP-Plus Profilometer from Ambios, mapping a surface area of 0.25 mm^2, and repeating the test up to 3 times for N80, N120 and CP samples.

3.3 Mechanical Characterization of Paper Substrates

Tensile tests were performed on the substrates on a traction machine from Rheometrics Scientific, model Minimat Firmware 3.1, equipped with a 20 N load cell. Substrates were cut with equal dimensions on the laser system and attached to the grips at a fixed distance that was measured, l_0. Tensile tests were performed at a velocity of 5 mm/min. Each test was repeated 5 times on 5 identical substrates.

3.4 Mechanical Characterization of Cantilevers

The mechanical characterization of the cantilevers via contact profilometry was perform on a XP-Plus Profilometer from Ambios. The stylus scanned the cantilever structures starting from the mark engraved so that the first millimetres corresponds to a flat surface, while the rest of the scan is performed on the suspended beam. The length of the scan was adapted to the specific cantilever length tested. Eight distinct load forces were applied (1.96, 4.9, 7.84, 9.8, 19.6, 49, 78.4, 98 μN) while recording the deflection. Five consecutive scans were performed for each scan force, ensuring also always the same scan position on the sample. In figure 4.6 (present in section 4.7), an image of the Stylus on a deflected cantilever can be seen.

3.5 Electrical Read-out

The following three different tests were conducted for the electrical read-out:

1. Inkej printing was performed using an PiXDRO LP50 printer by SUSS. Silver ink was used in Dimatix S-class cartridges for printing setting 1000 DPIs (drops per inch), a printing speed of 100 $mm.s^{-1}$, and a printhead height of 0.1 mm. After a single pass, the solvent was evaporated, and the ink was cured on a thermal plate at 140 °C.

2. Laser induced Graphene (LIG) was implemented on CP paper embedded with a 0.1 M solution of sodium tetraborate fire retardant, using the VLS 3.5 laser system using the settings described in annex II.4.

3. Screen printing of silver paste was performed on a manual system with a 77-mesh screen and a home-made stage.

4

Results and Discussion

Firstly, using a conventional micrometer, the thicknesses of the tested substrates were measured. The values presented table 4.1 result from the arithmetic mean (μ_T) of five replicated measurements for each substrate. The substrate with the highest thickness is the CP, while the one with the lowest thickness was the N80.

Table 4.1: The thickness of the substrate samples tested is denoted as μ_T, representing the average value, and σ_T, representing the standard deviation of the measurements.

T (μm)	PEN	N80	N120	CMN80	CMN120	WN80	WN120	CP
μ_T	81.8	63	90	74	110	108	143	163
σ_T	0.8	2	3	2	2	2	2	1.5

4.1 Characterization of Coated and Uncoated Paper Substrates

To analyze the nature of the used substrates (PEN, N80, N120 and CP), their surfaces were morphologically characterized through Scanning Electron Microscopy (SEM) and 3D profilometry. Furthermore, the N80 substrates coated with cellulose nanofibrils (denoted as Nanofibrillated cellulose membrane over Navigator paper 80g.m^{-2} substrate (CMN80)) and coated with wax (denoted as Wax coating over Navigator paper 80 g.m^{-2} substrate (WN80)) were also used in this study.

From SEM morphological characterization technique, the following images were obtained (figure 4.1). Upon initial visual inspection at the same magnification, it's clear that the polymeric film of PEN exhibit very low roughness. In contrast, the N80 and CP substrates appear to have higher roughness. Modified substrates, CMN80 and WN80, show an intermediate stage of surface modification, where the cellulose fiber network that makes up the substrate matrix is no longer discernible.

Through 3D profilometry, the average surface roughness (r) of the samples was quantified, represented as μ_r. The results are presented in the following table 4.2.

Given the high substrate roughness and the limited analyzed area (0.25 $\ll$ 5 mm^2), interpreting the table requires caution. As expected, the PEN film has a low average roughness of 420 nm. On the other hand, the roughest substrate is CP with an average

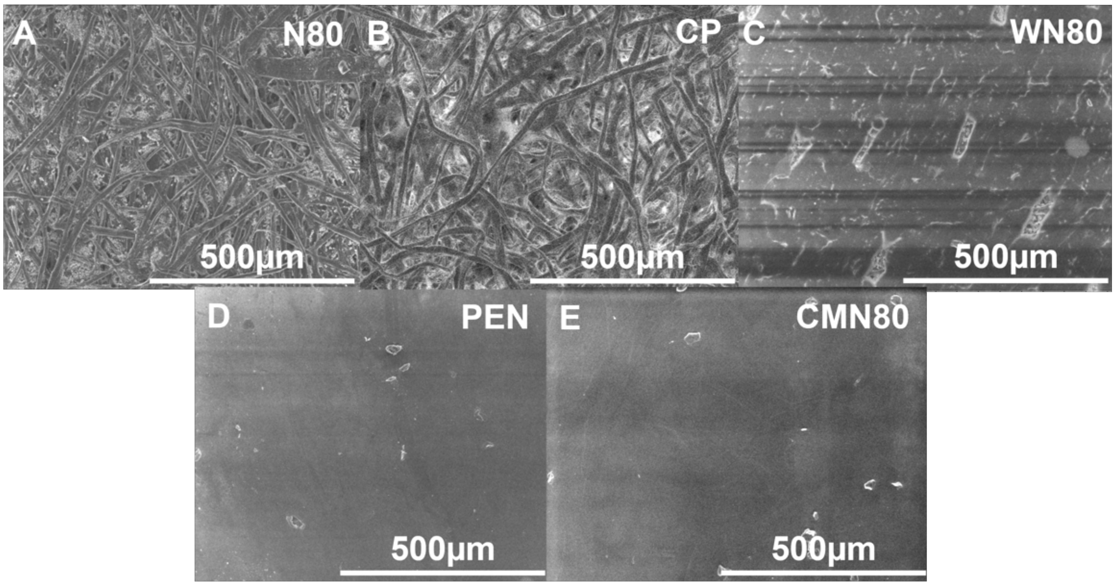

Figure 4.1: Top-view SEM micrographs of six substrate samples: (**A**) N80 sample, (**B**) CP sample, (**C**) WN80 sample, (**D**) PEN sample, (**E**) CMN80 sample.

Table 4.2: Roughness of different substrates samples

r (μm)	PEN	N80	N120	CMN80	WN80	CP
μ_R	0.42	3.92	2.78	1.21	2.31	10.37

roughness of 10.37 μm. Topographical profiles obtained using the same technique validate the previous analysis. In these figures (figure 4.2) , for the rougher substrates, leveling the profilometer stage was challenging since it was based on an extremely irregular reference substrate, potentially resulting in an artificial slope in the 3D profile.

In order to obtain a reference value for the expected elasticity of the cantilevers to be produced, tensile tests were conducted on the following substrates: N80, N120, CP, WN80, Wax coating over Navigator paper 120 g.m^{-2} substrate (WN120), CMN80, Nanofibrillated cellulose membrane over Navigator paper 120g.m^{-2} substrate (CMN120). The values, presented in table 4.3, are the arithmetic mean (μ_E) and the standard deviation (σ_E) of five replicates measured for each substrate.

The graphs 4.3 and 4.4 depict the relationship between stress and strain for the two sets of substrates, namely N80, N120, CP, and N80, WN80, and CMN80. The most accurate measure was conducted with CMN120 substrate, registering the lowest standard deviation of 0.05 GPa.

Since the following results were obtained by a tensile test and not through a bending test, these values should deviate from the expected the Young's modulus obtained through contact profilometry by an order of magnitude, according to the theory [26, 28].

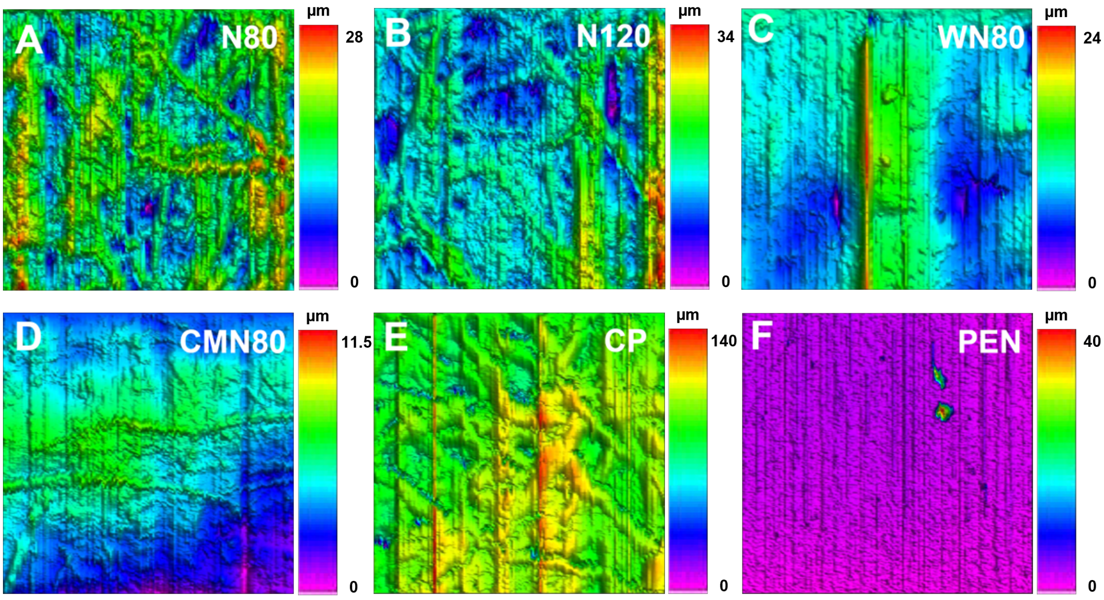

Figure 4.2: 3D profilometry scan of the samples surface: (**A**) N80 sample, (**B**) N120 sample, (**C**) WN80 sample, (**D**) CMN80 sample, (**E**) CP sample, (**F**) PEN sample.

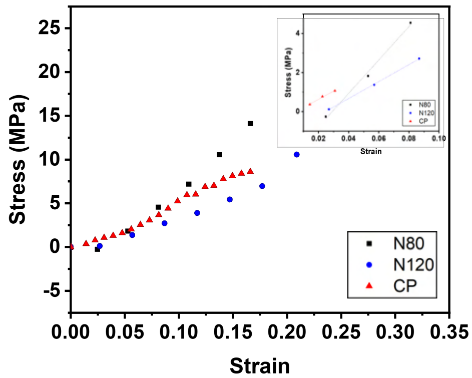

Figure 4.3: N80, N120 and CP graphical analysis, stress variation with strain ($\sigma s - S$) experienced by the substrates. Dash lines represent the linear regression for each set of data.

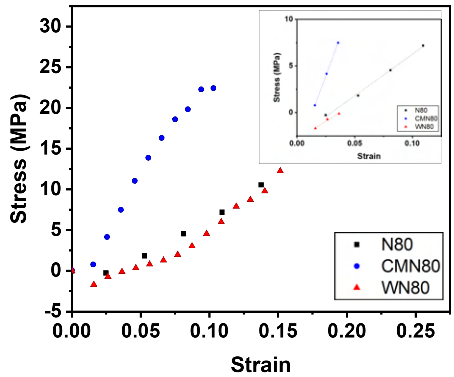

Figure 4.4: N80, CMN80 and WN80 graphical analysis, stress variation with strain ($\sigma_s - S$) experienced by the substrates. Dash lines represent the linear regression for each set of data.

Table 4.3: Substrates' Young's modulus obtained by tensile tests.

E (GPa)	N80	N120	CP	WN80	WN120	CMN80	CMN120
μ_E	0.087	0.15	0.05	0.2	0.15	0.38	0.29
σ_E	0.008	0.08	0.04	0.1	0.04	0.06	0.01

4.2 Layout and Geometry Considerations

The initial question to be addressed is the resolution of the equipment used in cantilever production, with the laser being the primary instrument that determines the achievable degree of miniaturization. In this initial study, the following substrates were used: N80 and N120.

In order to optimize the controllable parameters in the laser cutting system: power and beam speed. The goal was to reduce the presence of a brownish color effect that appeared when the cutting was overly energetic (figure 4.5.A), while still ensuring that the cut pattern on the substrate remained detached after completion. This methodology, due to the differences in the nature of the explored substrates, yielded different optimal combinations that allowed for clean cutting.

Table 4.4: Optimal laser cutting parameters combination. **(Left)** N80 combination, **(Right)** N120 combination.

Power (W)	Velocity (mm/s)
0.5	20.32
1	40.64

Power (W)	Velocity (mm/s)
0.5	11.43
1	20.32

The table 4.4 presents the optimized speed setting for a power of 0.5 W and 1 W for both papers studied N80 and N120. The most commonly used power setting was 0.5 W for both substrates. In exceptional situations (due to system malfunction issues), it was necessary to increase the power and cut at 1 W. These optimized conditions allow precise cutting without causing significant damage to the border regions of the paper.

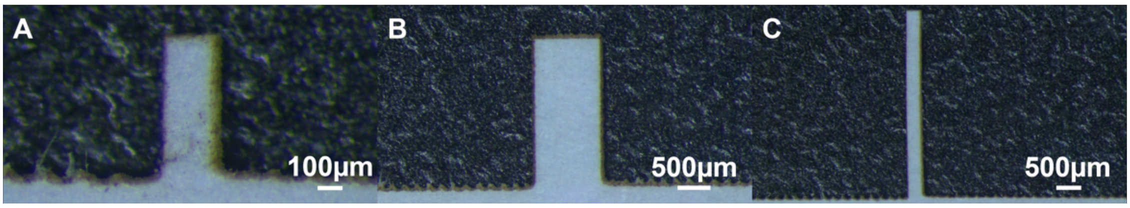

Figure 4.5: Photographs of several cantilevers produced. (**A**) 0.5x1 mm cantilever with the brownish effect on its border, (**B**) 1.5x3 mm cantilever, (**C**) 0.5x5 mm cantilever.

Different cantilevers were produced varying both the widths and the lengths (W= 0.5, 1, 1.5, 2, 2.5 and L = 1, 2, 3, 4, 5) where some can be seen in figure 4.5.B and figure 4.5.C.

To quantify the precision of laser cutting, a comparison was made between the final dimensions of the cantilevers and the dimensions initially present in the software produced layout. The following table 4.5 illustrates the percentage error (δ) between the layout values and the real dimensions of the produced.

The above data confirm the following trend: the percentage error decreases as the dimensions increase. For both substrates, a significant increase in error can be observed for cantilevers with a width of 0.5 mm compared to the others, reinforcing the idea that at this dimension, the resolution of the equipment is already being pushed to its limits.

Table 4.5: Percentage error between the layout and the real cantilevers.

	W (mm)					L (mm)				
Layout	**0.5**	**1**	**1.5**	**2**	**2.5**	**1**	**2**	**3**	**4**	**5**
N80	0.40	0.93	1.37	2.07	2.28	0.80	1.88	2.87	3.83	4.60
δ(%)	20.0	6.8	8.5	9.8	8.7	20	6.2	4.2	4.2	8.1
N120	0.42	0.94	1.34	1.84	2.27	0.82	1.87	2.86	3.84	4.78
δ(%)	16.0	6.0	11.0	8.0	9.0	18.0	7.0	5.0	4.0	5.0

The width that shows the most potential will be 1 mm, and the most interesting length, considering the implementation of the electrical read-out system, will be 5 mm.

4.3 Preliminary Cantilever Mechanical Characterization

Initially, the goal was to determine if it is possible to measure intermediate deflections in cantilevers with longer lengths. To achieve this, a cantilever with 1x4 mm (C4) was fabricated on an N80 substrate. Additionally, a second platform with the same width but a length of 10 mm (C10) was also produced using the same substrate. The elastic constant of both cantilevers was calculated using the mathematical expressions presented earlier (equation 2.2).

Table 4.6: Comparison between mechanical properties of C4 and C10.

	m ($m.N^{-1}$)	k_c ($N.m^{-1}$)
C4	0.5	1.8
C10	0.6	1.9

The detailed data necessary for constructing the table 4.6 is enclosed in the annex II.5.

Considering C4 as the reference, the measurement of deflection at 4 mm for both devices proved to be very close, with a percentage deviation between the final elastic constants of approximately 6% (table 4.6). These results enable the optimization of measurements for cantilevers with different geometries by keeping the width constant and interpolating the length along the deflection curves extracted from contact profilometry.

To determine the cantilever geometry, various cantilevers with different dimensions were tested on the profilometer varying the applied force during the stylus scan as referred on section 3.4.

Mechanical tests were conducted on the profilometer with cantilevers of different widths (W = 0.5 mm and W = 1 mm) and a fixed length of 10 mm. Deflections at 2, 3, 4, 5 mm were analyzed (figure 4.6). The elastic constant of the devices was calculated (table 4.7).

As can be seen from (figure 4.6), even though the cantilever exhibits high roughness, the deflection of the cantilever increases as the stylus moves through its length, and a clear dependence on the applied force is evident. It is also possible to observe that for a force of 10 mgF (98 μN) the bending of the cantilever exceeds the vertical range allowed

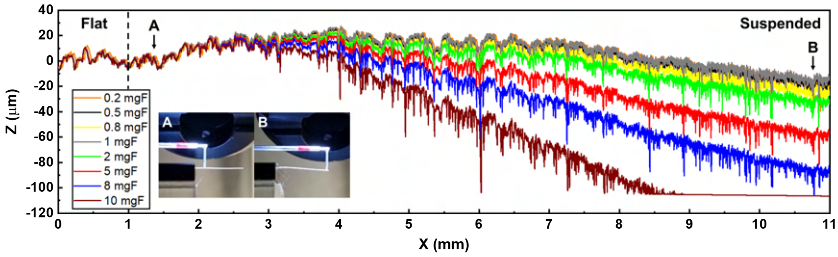

Figure 4.6: Scanning profile of N80 cantilever with 1x10mm.**(A)**Photo of the first moment of the scanning, no deflection recorded. **(B)** Photo of the last moment of the scanning, deflection is visible.

Table 4.7: Mechanical characterization for different N80 cantilevers.

W (mm)	L (mm)	m (m.N^{-1})	k$_c$ (N.m^{-1})
0.5	2	0.24	4.15
0.5	3	0.60	1.68
1	3	0.30	3.36
1	4	0.58	1.72
1	5	0.60	1.66

(predefined as 100 μm). Furthermore, due to the high roughness on the materials' surface, an approach to coating the substrates was proceed.

These preliminary results show that it is possible to detect the influence of the applied force on the deflection but to achieve better result the coating is necessary. Moreover, for further studies the geometry of the cantilevers were fixed at 1x5 mm (WxL).

4.4 Raw Cantilevers Bending Tests

After defining the cantilever geometry and creating several cantilevers in different materials (PEN, N80, N120 and CP), the mechanical characterization was conducted. This process involved determining deflections through mechanical tests carried out on the profilometer at the end of each platform. The data was processed to obtain deflection curves as a function of applied force, perform linear regression, and calculate physical parameters such as the the cantilever's elastic constant and Young's modulus.

The five replicas performed on different cantilevers (C_1, C_2, C_3, C_4, C_5) were used to individually calculate the average values of following parameters k$_c$ and E (μ_{kc} and μ_E) and subsequently the standard deviations associated (σ_{kc} and σ_E). The complete data regarding each replica, as well as the recorded average deflections, can be found in annex's section II.5.

For each sample, two graphs will be presented. The first graph illustrates the experienced deflection (Z deflection as a function of displacement). The second graph displays the deflections from the five replicas along with the lines representing their respective linear regressions.

In the graphical depiction of deflection concerning applied force, specific graphs feature data points that display negative deflections.These points emerge after normalizing the deflections obtained when the minimum force, 1.98 μN, was applied. Therefore, the negative points arise from scans where the stylus ended slightly above the reference scan, a consequence of the surface irregularity of the substrates under analysis.

The graphs figure 4.8 pertains to the deflection as a function of applied force for PEN and CP cantilevers.

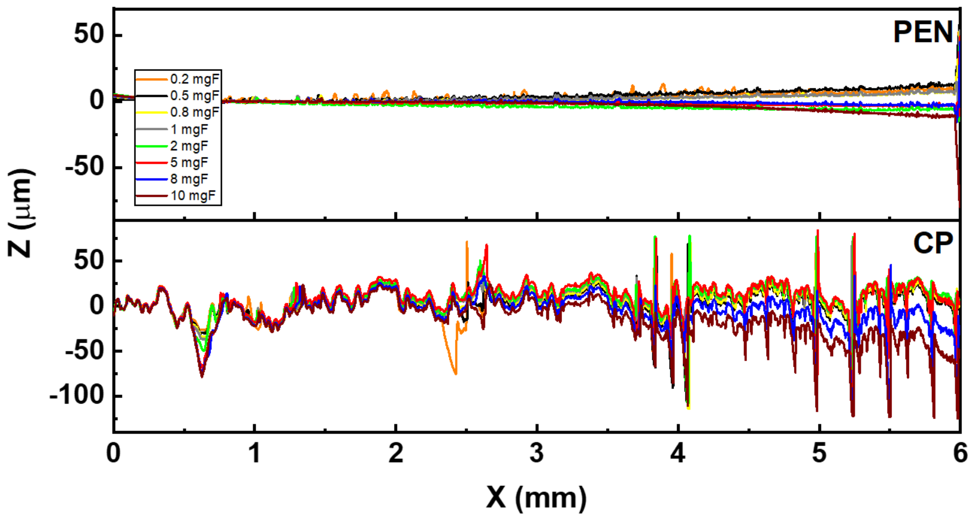

Figure 4.7: Cantilever scanning profile, Z axis position with stylus displacement ($Z - X$). **(Top)** PEN C3 cantilever, **(bottom)** CP C1 cantilever.

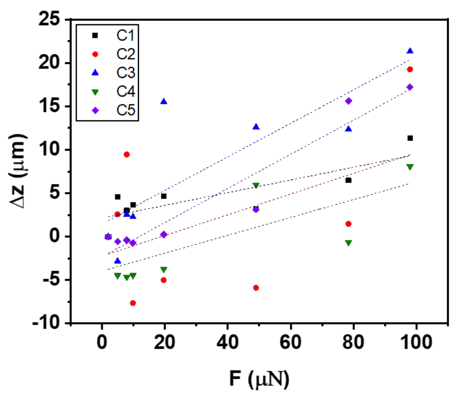

Figure 4.8: PEN graphical analysis, deflection variation with applied force ($\Delta z - F$) of PEN 1x5 mm cantilever. Dash lines represent the linear regression for each set of data.

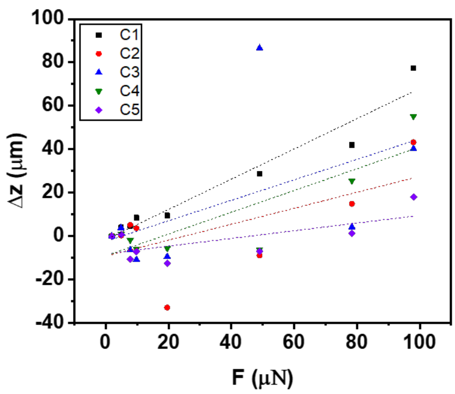

Table 4.8: CP graphical analysis, deflection variation with applied force ($\Delta z - F$) of CP 1x5 mm cantilever. Dash lines represent the linear regression for each set of data.

The use of PEN as a substrate was chosen to conduct an ideal mechanical analysis or reference study. Due to its low roughness, PEN is expected to exhibit linear deflection curves and, consequently, more accurate results figure 4.7.

The mechanical characterization results of PEN can be found in table 4.9. The average elastic constant of PEN cantilevers is 8 $N.m^{-1}$ and the average Young's modulus is 8 GPa. Additionally, variation in devices was observed due to the production process, resulting in the manufacturing of cantilevers with a range of elastic constants between 4 and 12 $N.m^{-1}$.

PEN is also a stiffer substrate, and the structures produced showed minimal deflections within the applied force range. This made the characterization of these devices challenging, explaining the variation in the results presented in the table 4.9.

Moreover, concerning the structures produced in this material, it's important to note that the cantilever dimensions are different due to laser cutting, which melts the polymer and produces a different effect compared to paper. This phenomenon explains the slight upper bending present in the final part of the cantilever for lower forces applied.

Concerning the CP substrate, its unique characteristics posed challenges for analysis. Figure 4.8 depicts the deflection as a function of applied force. From the table 4.9 average results, the elastic constant of CP cantilevers is 3 $N.m^{-1}$ and the Young's modulus is 0.3 GPa.

It is important to notice, from a relative perspective, this is the data has higher standard deviation values. In the manufacturing process, a diverse array of cantilevers with elastic constants ranging from 1 to 5 $N.m^{-1}$ was observed due to variations in devices resulting from the production process. It's important to note that the inherent roughness of the substrate introduces errors in the measurement. The graph 4.7 enables a comparison between the profile of a smooth substrate and the profile of the roughest substrate used in this study.

Characterizing N80 and N120, which serve as the primary matrices for the devices, was of particular importance.

Regarding the N80 and N120 cantilevers, the graph figure 4.9 represents a characteristic bending curve of the material.

The plots figure 4.10 pertain to the deflection as a function of applied force. From the table 4.9 average results, the elastic constant of N80 cantilevers is 2 $N.m^{-1}$ and the Young's modulus is 4 GPa. Furthermore, discrepancies in device characteristics were noted as a consequence of the manufacturing procedure, leading to the production of cantilevers exhibiting a diverse range of elastic constants spanning from 1 to 3 $N.m^{-1}$.

Regarding N120 cantilevers, the plots in figure 4.11 pertain to the deflection as a function of applied force. From the table 4.9 average results, the elastic constant of N120 cantilevers is 3 $N.m^{-1}$ and the Young's modulus is 2.5 GPa. Again, the production process yielded a spectrum of cantilevers characterized by varying elastic constants, with values falling within the range of 2 to 4 $N.m^{-1}$.

Despite the signal noise present in both cases, it's possible to observe an increase in stiffness in the higher density paper, resulting in a decrease of 45.1% in Young's modulus. As there wasn't a predefined application, the stiffer substrate was not excluded from further tests. Hence, the comparison between N80 and N120 continues through most of the experimental work.

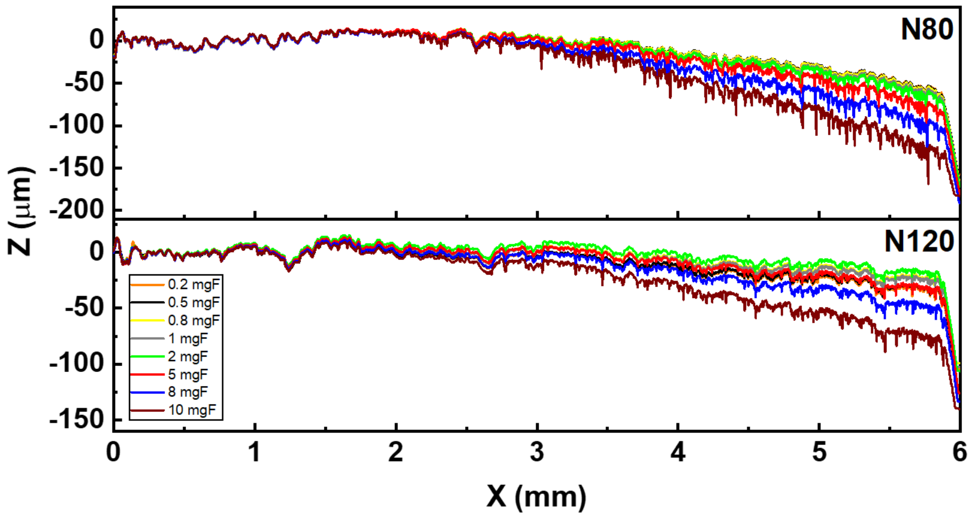

Figure 4.9: Cantilever scanning profile, Z axis position with stylus displacement ($Z - X$). **(Top)** N80 C1 cantilever, **(bottom)** N120 C1 cantilever.

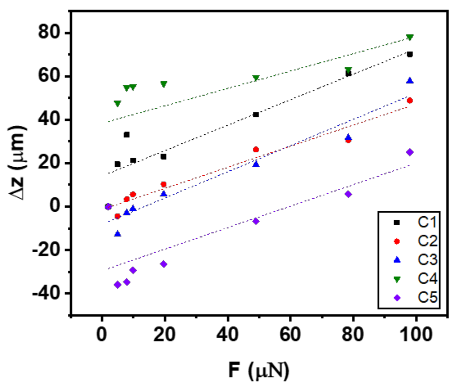

Figure 4.10: N80 graphical analysis, deflection variation with applied force ($\Delta z - F$) of N80 1x5 mm cantilever. Dash lines represent the linear regression for each set of data.

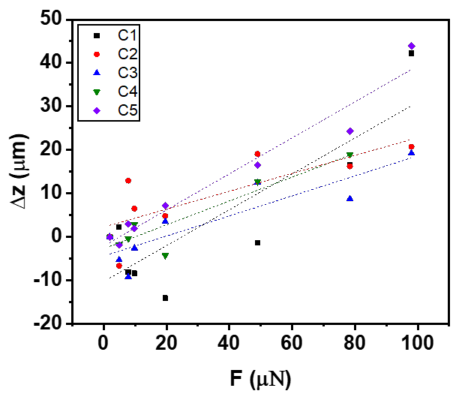

Figure 4.11: N120 graphical analysis, deflection variation with applied force ($\Delta z - F$) of N120 1x5 mm cantilever. Dash lines represent the linear regression for each set of data.

Table 4.9: Cantilevers mechanical characterization.

	k_c (N.m^{-1})		E (GPa)	
	μ_{kc}	σ_{kc}	μ_E	σ_E
PEN	8	4	8	3
N80	2	1	4	2
N120	3	1	2.5	0.8
CP	3	2	0.3	0.19

Concluding, due to its high porosity, CP exhibited a very rough profilometric signal with limited deflection. Therefore, the data obtained from tensile tests becomes crucial as it validates the previous analysis (present in section 4.1). Table 4.9 allows us to identify PEN as the stiffest substrate, while the most porous substrate, CP, exhibits lower stiffness and higher dispersion in the results, reinforcing the idea that the contact profilometry technique is more effective for less rough substrates. The commercial paper substrates show similar stiffness; however, the N120 cantilever records lower stiffness.

4.5 Coated Cantilevers Bending Tests

To reduce the error associated with deflection extraction, originating from surface roughness, the study of substrates with modified surfaces was conducted.

These substrates, with a coated wax surface, yielded the following results.

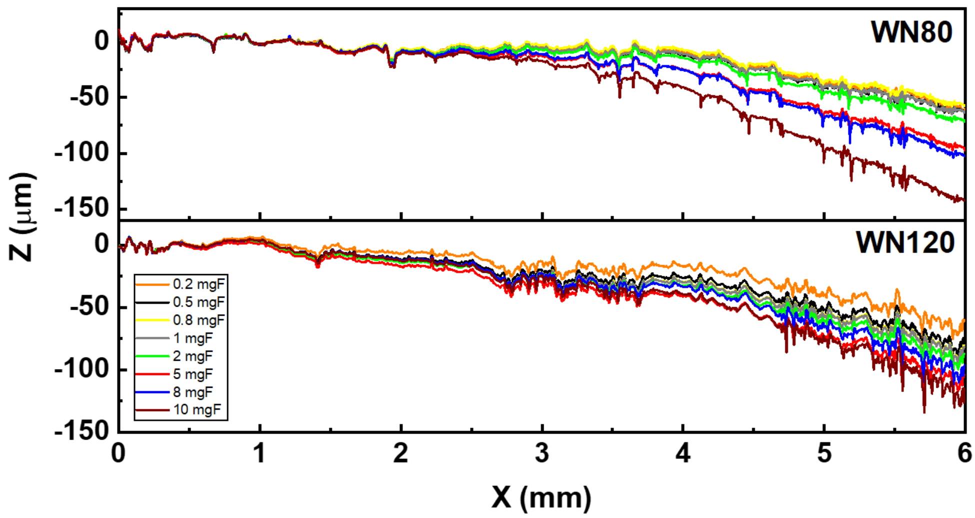

Figure 4.12: Cantilever scanning profile, Z axis position with stylus displacement ($Z - X$). **(Top)** WN80 C1 cantilever, **(bottom)** WN120 C2 cantilever.

In reference to the WN80 and WN120 cantilevers, figure 4.12 represents a characteristic bending curve for both materials.

Regarding WN80, the plots figure 4.13 pertain to the deflection as a function of applied force. From the table 4.10 average results, the elastic constant of WN80 cantilevers is 1.5 $N.m^{-1}$ and the Young's modulus is 0.6 GPa. Additionally, there was observed a device variation stemming from the production process, leading to the manufacturing of cantilevers with an elastic constant spanning from 1.2 to 1.8 $N.m^{-1}$.

Concerning the WN120 cantilevers, the plots from figure 4.14 show the deflection as a function of applied force. From the table 4.10 average results, the elastic constant of WN120 cantilevers is 2.8 $N.m^{-1}$ and the Young's modulus is 0.5 GPa. Furthermore, there

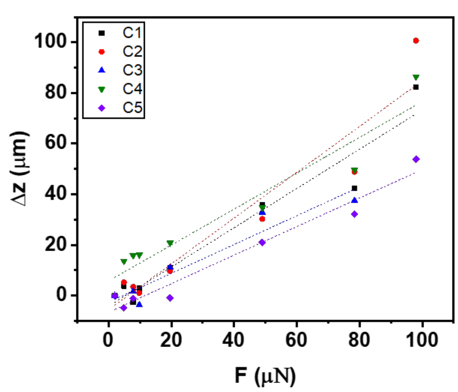

Figure 4.13: WN80 graphical analysis, deflection variation with applied force ($\Delta z - F$) of WN80 1x5 mm cantilever. Dash lines represent the linear regression for each set of data.

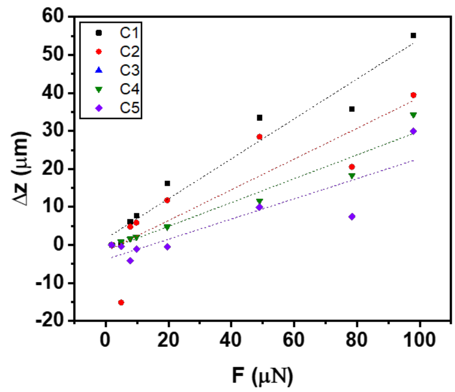

Figure 4.14: WN120 graphical analysis, deflection variation with applied force ($\Delta z - F$) of WN120 1x5 mm cantilever. Dash lines represent the linear regression for each set of data.

was a device variation linked to the production process, leading to the manufacture of cantilevers with an elastic constant fluctuating within the range of 2 to 3.6 N.m^{-1}.

The obtained signal profile indicates a reduction in surface roughness, achieving the initial objective. These substrates are also notable for their straightforward and rapid synthesis. Moreover, the cantilever's elastic constant has changed. Comparing the variation between N80 and N120 with the variation observed for WN80 and WN120, we can observe that the elasticity for WN80 experienced a significant reduction of 25% from the N80 device. In contrast, the WN120 device decreased by only 6% relative to the N120 cantilever.

To study the influence of wax on N80 and N120, the wax quantity per cantilever was studied, and the results are provided in annex I.1. As the study suggests, the WN80 substrate has a thicker layer of deposited wax. Therefore, the 7 percentage-point difference can be attributed to the varying amounts of wax deposited on the WN80 and WN120 cantilevers.

For cantilevers coated with a nanofibrillated cellulose membrane produced, the following results were obtained. Regarding the CMN80 and CMN120 cantilevers, the graph figure 4.15 represents a characteristic bending curve ofor both materials.

For CMN80 structures, the plots figure 4.16 pertain to the deflection as a function of applied force. From the table 4.10 results, the average elastic constant of CMN80 cantilevers is 1.1 N.m^{-1} and the Young's modulus is 2.3 GPa. Additionally, there was a variation in devices associated with the production process, resulting in the manufacture of cantilevers with an elastic constant variation ranging from 1.1 to 2.5 N.m^{-1}.

Regarding to the CMNN120 cantilevers,the plots figure 4.17 pertain to the deflection as a function of applied force. From the table 4.10 average results, the elastic constant of CMN120 cantilevers is 7 N.m^{-1} and the Young's modulus is 3 GPa. Furthermore, a

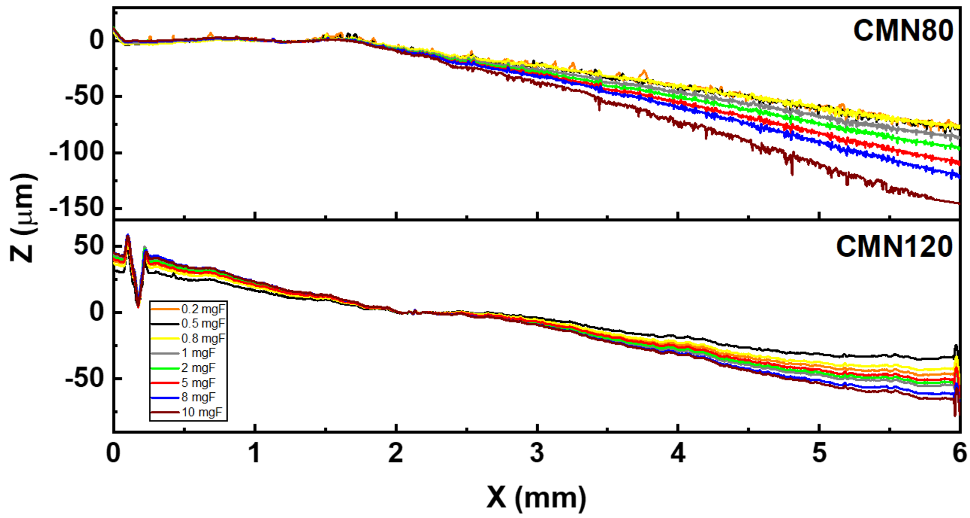

Figure 4.15: Cantilever scanning profile, Z axis position with stylus displacement ($Z-X$). **(Top)** CMN80 C2 cantilever, **(bottom)** CMN120 C4 cantilever.

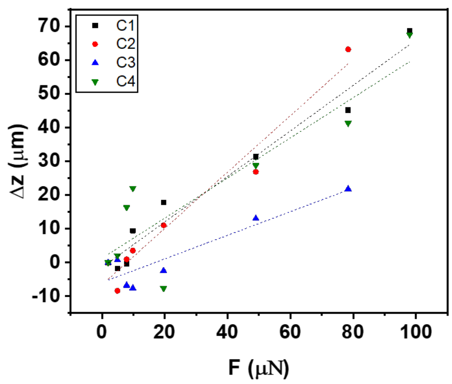

Figure 4.16: CMN80 graphical analysis, deflection variation with applied force ($\Delta z-F$) of CMN80 1x5 mm cantilever. Dash lines represent the linear regression for each set of data.

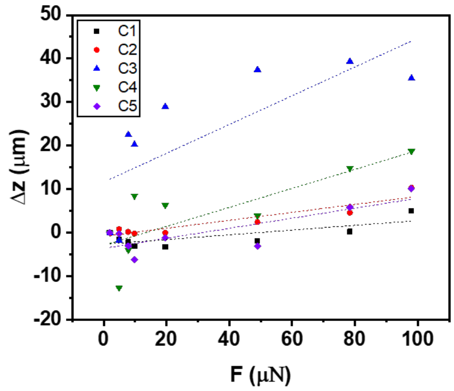

Figure 4.17: CMN120 graphical analysis, deflection variation with applied force ($\Delta z-F$) of CMN120 1x5 mm cantilever. Dash lines represent the linear regression for each set of data.

variation in devices was recorded due to the production process, resulting in the creation of cantilevers with an elastic constant ranging between 3 and 11 $N.m^{-1}$.

Table 4.10: Cantilevers mechanical characterization.

	k_c ($N.m^{-1}$)		E (GPa)	
	μ_{kc}	σ_{kc}	μ_E	σ_E
WN80	1.5	0.3	0.6	0.1
WN120	2.8	0.8	0.5	0.1
CMN80	1.8	0.7	2.3	0.9
CMN120	7	4	3	1

Regarding Table 4.10, it can be concluded that the results for the coated substrates show less dispersion, confirming the idea that the contact profilometry technique is more effective for smoother substrates. It is also noteworthy that substrates with the cellulose membrane are stiffer than the substrates with the wax coating.

Moreover, the cantilever's elastic constant has changed. When comparing the differences between N80 and N120 with those observed in CMN80 and CMN120, it's evident that the elasticity of CMN80 decreased by 10% compared to the N80 device. In contrast, the CMN120 device experienced a 130% increase relative to the N120 cantilever. This last conclusion should be approached with caution since there is also a significant variation in the k_c values among the CMN120 devices.

The CMN80 and CMN120 substrates have some disadvantages, such as high surface tension on one side of the membrane and the resulting curvature of the substrate at the boundary regions. The magnitude of this effect changes between devices, which explains the higher standard deviation values than initially expected.

This phenomenon was addressed by producing larger substrates, that increased production time. Additionally, cutting the most curved regions made the substrate flatter. Another strategy, not explored in this work, would involve producing a bi-layer of nanofibrillated cellulose, attempting to cancel out the membrane's surface tension with another symmetrical tension, i.e creating a neutral point. This approach would consume more time, and the surface production of the second membrane would only serve a structural purpose, not directly related to the intended surface smoothing.

In summary, CMN80 and CMN120 exhibit the least rough surfaces and are thus the most promising for further experimental work.

In this work, the influence of paper orientation during laser cutting was also studied, as detailed in annex I.3.

4.6 Electrical Readout Circuit

The designed read-out system for the cantilevers consisted of a small track running up to half of the platform and connected to two electrodes, where the resistance variation would be measured through the piezoresistive effect, already studied ([33, 47, 48]). To ensure a fair comparison, a reference design was created in Adobe Illustrator. The deposition of electrodes was studied using inkjet (section 4.6.1), screen printing (section 4.6.3), and LIG techniques (section 4.6.2).

Moreover, CMN80 was chosen as the substrate for further work due to its lower roughness and greater deflection.

4.6.1 Inkjet Printing

Inkjet printing, as a deposition technique, showed promise due to its high precision and reproducibility as an automated process. However, this technique presented challenges related to the type of printing substrate, which affected deposition performance.

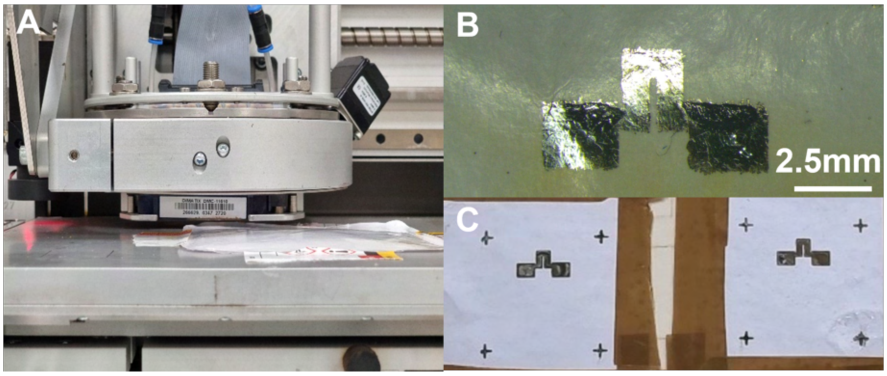

Figure 4.18: Inkjet photographic record. (**A**) Inkjet printer working on a wrinkled CMN80 substrate, (**C**) Inkjet printing after thermal curing of the ink. It can be noticed a yellow tone appearing in CMN80 due to substrate degradation, (**D**) Inkjet printing samples ready to laser cut stage.

CMN80 exhibited small irregularities, a result of the surface tension of the nanofibrillated cellulose membrane. These irregularities prevented proper flat fixation of the substrate on the printing stage, leading to varying distances between the nozzle and the substrate during printing and deteriorating print quality (figure 4.18.B).

Additionally, the silver ink used required curing at 220 °C for 30 min. Since CMN80's integrity is compromised at this temperature, a compromise at 140 °C was attempted for the same duration. However, this led to two negative effects affecting read-out system production. Firstly, curing at a lower temperature than suggested proved ineffective, resulting in overly resistive tracks and electrodes, making terminal electrode reading unfeasible. The second issue arose from the substrate wrinkling during placement on the heating plate for ink curing, disrupting the original fiber orientation and being irreversible (figure 4.18.C).

Despite these challenges, optical microscopy measurements were performed on the manually printed system, which provided valuable insight. The resolution of the printing was the greatest among the other techniques. However, this feature does not change its poor electrical conductivity.

4.6.2 Laser Induced Graphene

In Laser Induced Graphene (LIG), a range of power and speed combinations was tested, yielding the following data (figure 4.19).

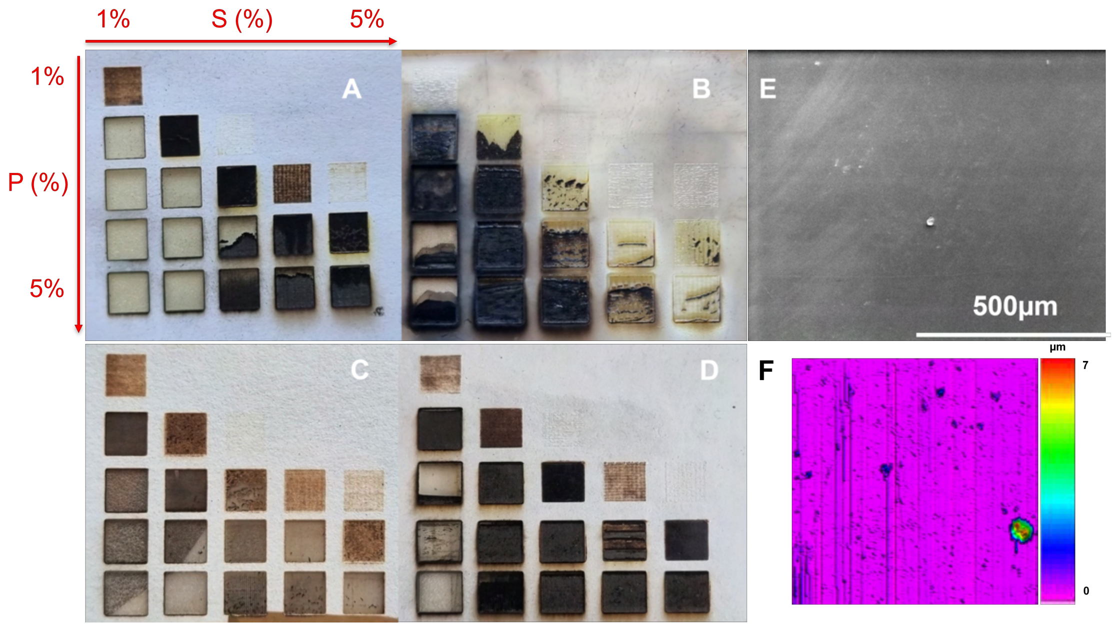

Figure 4.19: Laser induced graphene study on different substrates. Each square corresponds to a matrix combination of speed (S) with power (P), varying percentage units between 1% and 5%. (**A**) LIG on N80 with P-C coating, (**B**) LIG on PEN with P-C coating, (**C**) LIG on FRCP, (**D**) LIG on CMN80 with P-C coating, (**E**) P-C SEM image, (**F**) P-C 3D Profilometry image

LIG on paper appears to be the more practical technique due to its integration with the laser cutting process. However, the use of a rougher substrate and chemical treatment affects the mechanical properties of the substrate, discussed in the annex section I.2. A second approach could involve the production of graphene using Parylene-C substrate (P-C).

To begin this process, the Parylene film was first characterized morphologically (figures 4.19.E and 4.19.F). The parylene film has an average thickness of 33 μm and a mean roughness of 552 nm.

The parylene-based LIG method offers the advantage of using the ideal CMN80 substrate with a parylene coating. Nevertheless, this method is more complex, time-consuming, and requires equipment capable of handling high vacuum conditions.

Moreover, it was observed the duplication of the Stoney's effect, with the presence of two interfaces (from the substrate to the cellulose membrane and from the cellulose membrane to the parylene film) generating surface tensions that modify the final deflection of the cantilever.

Furthermore, the laser cutting equipment had some regularity issues, with power variations depending on the cutting direction, suggesting a need for more regular and careful maintenance.

4.6.3 Screen Printing

Screen printing proved the most promising technique due to its better results. In the initial approach to this technique, the printing mask's dimensions and the choice of substrate were studied. The dimensions of tracks and electrodes were minimized to maintain good resolution while respecting cantilever limitations. Masks were tested using kapton tape and PEN as substrates.

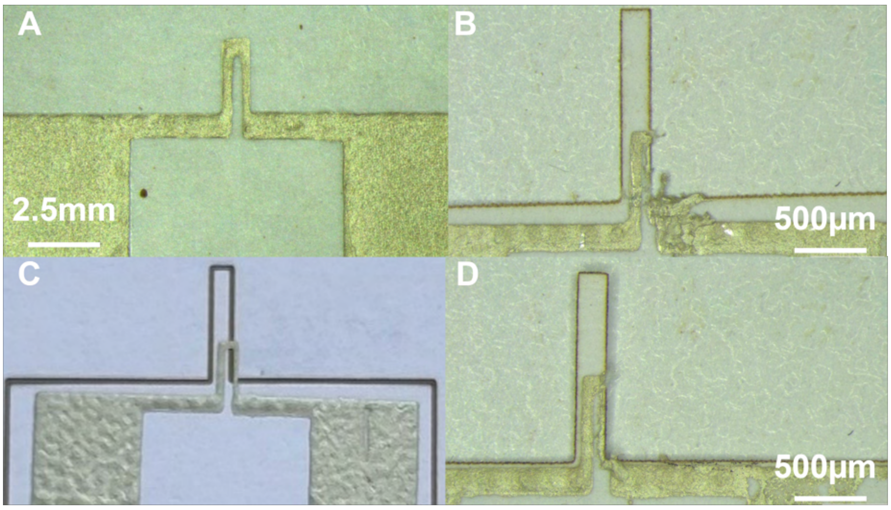

Figure 4.20: Inkjet photographic record. (**A**) Screen printed deposition sample, (**D**) Poorly needle correction of the screen printing pattern, (**F**) Misalignment between the print and the cut, (**G**) Ideal needle correction of the screen printing pattern.

Kapton tape presented problems during laser cutting. At the intended resolution, it couldn't produce functional masks due to the adhesive force between the tape and the glass substrate, leading to tearing during mask detachment. PEN was considered, given its previous use in mechanical characterization of cellulose cantilevers, providing optimized laser cutting for high-quality mask production.

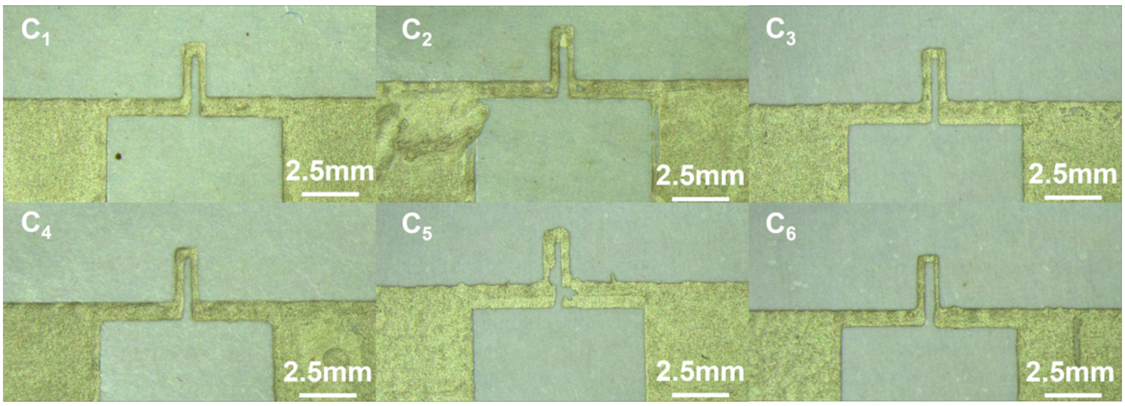

Figure 4.21: Six screen printing replicas on CMN80 substrates.

PEN, however, had a thickness 36.67% times greater than kapton tape. During deposition, this affected print quality as the mechanical behavior of the ink depended on printing force, speed, and channel length ink had to traverse. Thicker substrates increased the channel length, making technique replicability more challenging.

For both inkjet and screen printing, as they are electrode deposition techniques independent of laser cutting, a procedure order had to be established. Either substrate cutting preceded pattern printing, or the order was reversed. The first approach is complex for inkjet and impossible for screen printing due to the dimensions of the cut and the confined platform. Additionally, fixing cellulose substrates to the stage posed challenges.

Therefore, for both inkjet and screen printing, the substrate was printed first, followed by laser cutting. Reference marks were added to the pattern to facilitate substrate alignment with the designed electrical system. Despite fixed dimensions, commercial equipment characteristics and stage irregularities made substrate alignment challenging, affecting the final cut of a functional device that would conduct between electrodes. Moreover, the conduction layer had different cutting resistance than the substrate, sometimes leading to successful substrate cutting but unsuccessful cutting of regions containing tracks. As shown in figure 4.20.C depict the aforementioned difficulties.

4.7 Proof of Concept

The first results in the electrode deposition phase led to the suspension of work. To achieve the main objective of creating cellulose substrate cantilevers, the geometry was redefined, the best substrate (CMN80) was chosen, mechanical characterization was performed, the best electrode deposition technique (screen printing) was selected, and the resistance between electrodes was characterized.

4.7.1 Geometry Considerations

Expanding the base of the platform was necessary to continue the project. The new Proof of concept cantilever (POC) now have a base of 2 mm and a length of 5 mm (figure 4.11). Doubling the base allowed for more error margin during substrate alignment with the printed patterns.

4.7.2 Mechanical and Electrical Characterization

As expected, the raw new structures exhibited less deflection. The characterization of cantilever C5 was flawed, leading to its exclusion from the subsequent analysis.

With respect to POC and ePOC cantilevers, the graph figure 4.23 represents a characteristic bending curve of both cantilevers.

The plots figure 4.24 pertain to the deflection as a function of applied force. From the table 4.12 average results, the elastic constant of 2x5 mm cantilevers is 5 N.m and the Young's modulus is 3 GPa. There was a variation in devices associated with the

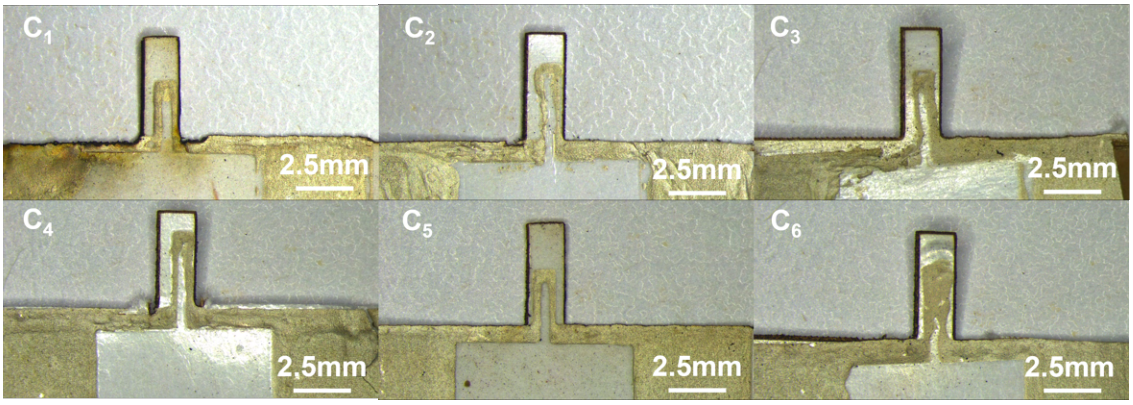

Figure 4.22: Six POC replicas.

Table 4.11: Dimension characterization based on annex's figure II.18.Each letter corresponds to a specific and identified distance in the diagram. The measurements marked with * for f and g do not apply to the mask.

	Layout (mm)	Mask (mm)	μ (mm)	σ (mm)
a	0.91	1.10	1.02	0.13
b	0.25	0.44	0.73	0.23
c	4.09	3.31	3.43	0.44
d1	0.15	0.40	0.36	0.08
d2	0.15	0.45	0.41	0.10
e1	0.70	0.95	0.89	0.21
e2	0.70	0.91	0.86	0.09
f	5.00	*	4.68	0.26
g	2.00	*	1.59	0.25

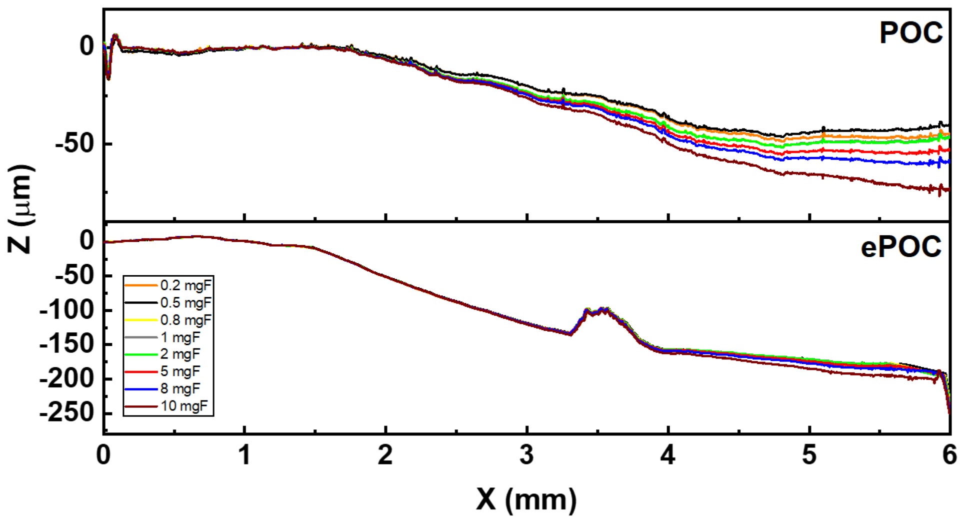

Figure 4.23: Cantilever scanning profile, Z axis position with stylus displacement ($Z - X$). **(Top)** POC C1 cantilever, **(bottom)** ePOC C3 cantilever.

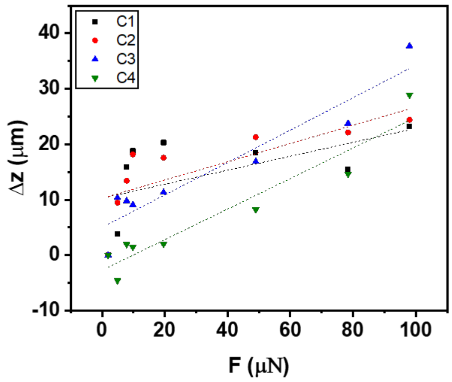

Figure 4.24: POC graphical analysis, deflection variation with applied force ($\Delta z - F$) of POC 1x5 mm cantilever. Dash lines represent the linear regression for each set of data.

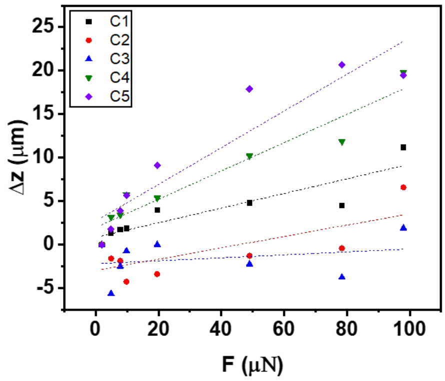

Figure 4.25: ePOC graphical analysis, deflection variation with applied force ($\Delta z - F$) of ePOC 1x5 mm cantilever. Dash lines represent the linear regression for each set of data.

Table 4.12: POC and ePOC cantilevers mechanical characterization.

	k_c (N.m^{-1})		**E (GPa)**	
	μ_{kc}	σ_{kc}	μ_E	σ_E
POC	5	2	3	1
ePOC	9	5	6	3

production process, leading to the manufacturing of cantilevers with an elastic constant ranging between 3 and 7 N.m^{-1}.

As for the Proof of concept with printed electrodes cantilever (ePOC), in graph figure 4.23, is possible to observe the profile of the silver track deposited on the cantilever at 3.5 mm. The plots figure 4.25 pertain to the deflection as a function of applied force.

From the table 4.12 average results, the elastic constant of the printed electrodes cantilevers is 9 N.m^{-1} and the Young's modulus is 6 GPa. There was a variance in devices due to the production process, resulting in the creation of cantilevers with an elastic constant ranging from 4 to 14 N.m^{-1}.

Concluding, the new structures exhibited less deflection due to their silver electrodes. Therefore, we can affirm that structures with deposited electrodes exhibit higher rigidity, with a Young's modulus ranging from 3 to 9 GPa. Consequently, the applied force range no longer allows differentiation of deflections. Similar to what was observed with PEN cantilevers in section 4.4, analyzing these cantilevers would require conducting a sweep with higher applied forces.

To finish the project, it was conducted an electrical characterization, more precisely, it was determined the resistance (R) between electrodes of ePOC, results are shown in table 4.13.

The created devices exhibit an average (μ_R) resistance of 260 Ω. The produced cantilevers are electrically conductive, exhibiting electrical resistance ranging from 110 Ω to

Table 4.13: ePOC resistance characterization.

R (Ω)	$\mathbf{C}_1$	$\mathbf{C}_2$	$\mathbf{C}_3$	$\mathbf{C}_4$	$\mathbf{C}_5$	$\mathbf{C}_6$	μ_R	σ_R
ePOC	340	280	220	100	120	500	260	150

410 Ω.

The variability in resistance among replicas stems from the production process; the manual aspect of screen printing doesn't guarantee optimal reproducibility.

5

Conclusions and Future Perspectives

This study was an ambitious experimental undertaking, leveraging a deep understanding of materials and the straightforward techniques employed in the production of cantilevers.

Paper is a highly versatile and environmentally friendly material compared to less eco-friendly substrates. In this work, various types of paper were studied, with differences in cellulose fiber density, chemical compositions, porosities, surface functionalizations, and, most importantly, mechanical properties. The versatility of these substrates can ultimately be summarized by their ability to be functionalized, chemically modified to serve a very specific mechanical purpose.

Despite the geometric adaptation of the devices to implement the transduction system, the cantilever has millimeter-sized dimensions that allow implementation in various sensory systems already mentioned in the introduction.

The future direction of this research involves electrical characterization as a function of mechanical deflection, necessitating the design of a system to facilitate this process. To achieve this, contact profilometry presents a more challenging technique, as it requires the tip to move along the cantilever, while a commercial multimeter is employed to monitor resistive variations through the characteristic piezoresistive effect in these sensors.

After determining the sensitivity of the sensor signal transduction to external forces, it will be important to define an application based on the intrinsic sensitivity of the sensor, as well as the functional layer responsible for receiving the analyte or the phenomenon to be detected. At this stage, it's crucial to revisit the setup for sensor sensitivity characterization. This new configuration could pose greater challenges if we aim to detect more complex analytes, such as enzymes and volatile organic compounds. On the other hand, we can try a simpler system and proceed with the measurement of temperature or humidity in a controlled atmosphere.

Regarding the optimization of the sensors themselves, there is still a long way to go. The proof-of-concept cantilever reached has significant room for improvement. First, the issue of surface tension resulting from the CMN80 membrane implementation. As mentioned earlier, there are several proposed solutions to minimize the problem. However, due to time constraints, we were unable to proceed with the optimization process for producing electrodes through LIG, being more rigorous is also more time-demanding than the method implemented. The ultimate goal of this work remains the integration of cantilever production and electrode creation into a single process, which would be a significant achievement. This is why we studied the production of cantilevers with a parylene film or the influence of the chemical bath on the mechanical properties of the structures. Continuing down this path would be highly interesting.

Second, another important aspect worth considering is the alignment and laser cutting of the substrates. The final cutting of the cantilevers after implementing the transduction circuit by one of the deposition techniques already studied could be done at anchor points, i.e., in areas where the silver electrodes could obstruct the cut and would not be admitted in the layout beforehand. These areas would have to be cut later with a blade, but it would allow for a cleaner cut and avoid the multiple laser passes required to cut the substrate with deposited silver.

Finally, an alternative to laser cutting could involve using an automated mechanical blade cutting system, where the desired layout was submitted to the equipment program, calibration of parameters (blade height, cutting speed, etc.) was performed, and the substrate would also be cut with the desired pattern. This solution would be very promising as it would replace a more energy-intensive and complex system, such as laser cutting, with a simpler and cheaper one.

In conclusion, this project culminates with a pronounced emphasis that has characterized the recent months of diligent effort, effectively delineating our forward-looking stance toward technology: reinvention. Just as we have innovatively reengineered microscale structures, we have similarly demonstrated the adaptability of more conventional techniques and equipment, ultimately contributing to the success of this endeavor.

Bibliography

[1] H.-Y. Kang and J. M. Schoenung. "Used consumer electronics: a comparative analysis of materials recycling technologies". In: *IEEE International Symposium on Electronics and the Environment, 2004. Conference Record. 2004*. IEEE. 2004, pp. 226–230 (cit. on p. 1).

[2] J. Yla-Mella, E. Pongrácz, and R. L. Keiski. "Recovery of waste electrical and electronic equipment (WEEE) in Finland". In: *Proceedings of the waste minimization and resource use optimization conference*. Vol. 10. 2004, pp. 83–92 (cit. on p. 1).

[3] U. ESCAP. "Sustainable Development Goal 12: ensure sustainable consumption and production patterns". In: (2016) (cit. on p. 1).

[4] I. Ilankoon et al. "E-waste in the international context–A review of trade flows, regulations, hazards, waste management strategies and technologies for value recovery". In: *Waste management* 82 (2018), pp. 258–275 (cit. on p. 1).

[5] P. Anastas et al. *The power of the United Nations sustainable development goals in sustainable chemistry and engineering research*. 2021 (cit. on p. 1).

[6] I. C. Nnorom and O. Osibanjo. "Overview of electronic waste (e-waste) management practices and legislations, and their poor applications in the developing countries". In: *Resources, conservation and recycling* 52.6 (2008), pp. 843–858 (cit. on p. 1).

[7] E. W. Nery and L. T. Kubota. "Sensing approaches on paper-based devices: a review". In: *Analytical and bioanalytical chemistry* 405 (2013), pp. 7573–7595 (cit. on pp. 3, 7).

[8] S. Ummartyotin and H. Manuspiya. "A critical review on cellulose: From fundamental to an approach on sensor technology". In: *Renewable and Sustainable Energy Reviews* 41 (2015), pp. 402–412 (cit. on pp. 3, 7).

[9] J. C. Roberts. *The chemistry of paper*. Royal Society of Chemistry, 2007 (cit. on p. 3).

[10] A. C. O'sullivan. "Cellulose: the structure slowly unravels". In: *Cellulose* 4 (1997), pp. 173–207 (cit. on p. 3).

[11] A. Ebringerová, Z. Hromádková, and T. Heinze. "Hemicellulose". In: *Polysaccharides I: Structure, characterization and use* (2005), pp. 1–67 (cit. on p. 4).

[12] A. Stepanov, E. Saukkonen, and H. Piili. "Possibilities of laser processing of paper materials". In: *Physics Procedia* 78 (2015), pp. 138–146 (cit. on p. 4).

[13] H. M. Piili. "Characterization of interaction phenomena of laser beam and paper". In: *Svensk papperstidning* 85.3 (1982), R1–R6 (cit. on p. 4).

[14] K. Tashiro and M. Kobayashi. "Theoretical evaluation of three-dimensional elastic constants of native and regenerated celluloses: role of hydrogen bonds". In: *Polymer* 32.8 (1991), pp. 1516–1526 (cit. on p. 4).

[15] S. Eichhorn and G. Davies. "Modelling the crystalline deformation of native and regenerated cellulose". In: *Cellulose* 13 (2006), pp. 291–307 (cit. on p. 4).

[16] R. E. Mark et al. "Cell wall mechanics of tracheids." In: *Cell wall mechanics of tracheids.* (1967) (cit. on p. 4).

[17] P. G. Dixon and L. J. Gibson. "The structure and mechanics of Moso bamboo material". In: *Journal of the Royal Society Interface* 11.99 (2014), p. 20140321 (cit. on p. 4).

[18] D. Kretschmann. "Wood handbook: wood as an engineering material". In: *General Technical Report FPL-GTR-190. US Department of Agriculture, Forest Service, Forest Products Laboratory* (2010) (cit. on p. 4).

[19] M. F. Qaseem, H. Shaheen, and A.-M. Wu. "Cell wall hemicellulose for sustainable industrial utilization". In: *Renewable and Sustainable Energy Reviews* 144 (2021), p. 110996 (cit. on p. 4).

[20] A. Milanez et al. "Influência das hemiceluloses nas propriedades óticas e físico-mecânicas da polpa". In: *XV Congresso Anual da ABCP: Semana do Papel*. ABTCP São Paulo. 1982, pp. 22–26 (cit. on p. 4).

[21] C. Schönberg et al. "The importance of xylan for the strength properties of spruce kraft pulp fibres". In: (2001) (cit. on p. 4).

[22] H.-J. Butt. "A sensitive method to measure changes in the surface stress of solids". In: *Journal of colloid and interface science* 180.1 (1996), pp. 251–260 (cit. on pp. 4, 6).

[23] G. Y. Chen et al. "Adsorption-induced surface stress and its effects on resonance frequency of microcantilevers". In: *Journal of Applied Physics* 77.8 (1995), pp. 3618–3622 (cit. on p. 4).

[24] J. Fritz. "Cantilever biosensors". In: *analyst* 133.7 (2008), pp. 855–863 (cit. on p. 5).

[25] G. Hua et al. "Poisson's ratios of molded pulp materials by digital image correlation method and uniaxial tensile test". In: *Journal of Engineered Fibers and Fabrics* 15 (2020), p. 1558925020908271 (cit. on p. 6).

[26] Y.-C. Tai and R. S. Muller. “Measurement of Young’s modulus on microfabricated structures using a surface profiler”. In: (1990) (cit. on pp. 6, 12).

[27] M. Denhoff. “A measurement of Young’s modulus and residual stress in MEMS bridges using a surface profiler”. In: *Journal of Micromechanics and Microengineering* 13.5 (2003), p. 686 (cit. on p. 6).

[28] J. He et al. “Mechanical characterization of biocompatible thin film materials by scanning along micro-machined cantilevers for micro-/nano-system”. In: *Materials Science and Engineering: A* 423.1-2 (2006), pp. 134–142 (cit. on pp. 6, 12).

[29] E. W. Lam. “Fabrication and material characterization of silver cantilevers via direct surface micromachining”. PhD thesis. Massachusetts Institute of Technology, 2008 (cit. on p. 6).

[30] N. V. Lavrik, M. J. Sepaniak, and P. G. Datskos. “Cantilever transducers as a platform for chemical and biological sensors”. In: *Review of scientific instruments* 75.7 (2004), pp. 2229–2253 (cit. on p. 7).

[31] S. K. Vashist. “A review of microcantilevers for sensing applications”. In: *J. of Nanotechnology* 3 (2007), pp. 1–18 (cit. on p. 7).

[32] C. Liu. “Recent developments in polymer MEMS”. In: *Advanced Materials* 19.22 (2007), pp. 3783–3790 (cit. on p. 7).

[33] S. Emamian et al. “Fabrication and characterization of piezoelectric paper based device for touch and force sensing applications”. In: *Procedia engineering* 168 (2016), pp. 688–691 (cit. on pp. 7, 23).

[34] D. D. Liana et al. “Recent advances in paper-based sensors”. In: *sensors* 12.9 (2012), pp. 11505–11526 (cit. on p. 7).

[35] X. Qin et al. “A paper based milli-cantilever sensor for detecting hydrocarbon gases via smartphone camera”. In: *Analytical Chemistry* 92.12 (2020), pp. 8480–8486 (cit. on p. 7).

[36] Z. Nie et al. “Electrochemical sensing in paper-based microfluidic devices”. In: *Lab on a Chip* 10.4 (2010), pp. 477–483 (cit. on p. 7).

[37] H. Heidari-Bafroui et al. “Development of a New Lab-on-Paper Microfluidics Platform Using Bi-Material Cantilever Actuators for ELISA on Paper”. In: *Biosensors* 13.3 (2023), p. 310 (cit. on pp. 7, 8).

[38] A. Fraiwan, H. Lee, and S. Choi. “A paper-based cantilever array sensor: Monitoring volatile organic compounds with naked eye”. In: *Talanta* 158 (2016), pp. 57–62 (cit. on pp. 7, 8).

[39] H. Heidari-Bafroui et al. “A Parametric Study on a Paper-Based Bi-Material Cantilever Valve”. In: *Micromachines* 13.9 (2022), p. 1502 (cit. on p. 7).

[40] A. Dukle et al. “Role of Paper-Based Sensors in Fight against Cancer for the Developing World”. In: *Biosensors* 12.9 (2022), p. 737 (cit. on p. 8).

[41] T.-L. Ren et al. “Flexible graphite-on-paper piezoresistive sensors”. In: *Sensors* 12.5 (2012), pp. 6685–6694 (cit. on p. 8).

[42] E. Hart. “Theory of the tensile test”. In: *Acta metallurgica* 15.2 (1967), pp. 351–355 (cit. on p. 8).

[43] D. Leguillon, É. Martin, and M.-C. Lafarie-Frenot. “Flexural vs. tensile strength in brittle materials”. In: *Comptes Rendus Mécanique* 343.4 (2015), pp. 275–281 (cit. on p. 8).

[44] M. Maalej and V. C. Li. “Flexural/tensile-strength ratio in engineered cementitious composites”. In: *Journal of Materials in Civil Engineering* 6.4 (1994), pp. 513–528 (cit. on p. 8).

[45] C. Guezennec. “Development of new packaging materials based on micro-and nano-fibrillated cellulose”. PhD thesis. PhD thesis, Université de Grenoble, 2012 (cit. on p. 9).

[46] H. Sehaqui et al. “Fast preparation procedure for large, flat cellulose and cellulose/inorganic nanopaper structures”. In: *Biomacromolecules* 11.9 (2010), pp. 2195–2198 (cit. on p. 9).

[47] L. Gao et al. “All paper-based flexible and wearable piezoresistive pressure sensor”. In: *ACS Applied Materials & Interfaces* 11.28 (2019), pp. 25034–25042 (cit. on p. 23).

[48] X. Liu et al. “based piezoresistive MEMS sensors”. In: *Lab on a Chip* 11.13 (2011), pp. 2189–2196 (cit. on p. 23).

PRINT / WEBOGRAPHY

[49] S. Kemp. *DIGITAL 2023: GLOBAL OVERVIEW REPORT*. 2023. URL: https://datareportal.com/reports/digital-2023-global-overview-report2 (visited on 2023-03-01) (cit. on p. 1).

[50] JRS. 2023. URL: http://www.jrs.eu/jrs%7B%5C_%7Den/%20innovative-functionality/functions-jrs-products/ (visited on 2023-03-05) (cit. on p. 5).

I

Complementary Studies

I.1 Wax Mass Coating Study

To assess whether the amount of wax deposited on the paper substrate is consistent, the following study was conducted on WN80 and WN120 samples. Laser-cut rectangular patterns measuring 172.19 mm^2 were created in the following materials: S_r(N80, N120) and S_w (WN80, WN120). Subsequently, each substrate was weighed, and by calculating the difference between substrates with and without wax, the mass of wax in each sample was determined. This mass was then normalized with respect to the previously calculated area, providing an estimate of the wax mass present in each cantilever.

m (mg)	$\mathbf{S}_r$	$\mathbf{S}_w$
1	13.2	14.8
2	13.1	15.4
3	13.1	15.1
4	13	15.2
5	13.3	15.5
μ_m	13.14	15.2
σ_m	0.11	0.27

m (mg)	$\mathbf{S}_r$	$\mathbf{S}_w$
1	20.3	21.8
2	20.5	21.3
3	20.5	22.1
4	21.1	22
5	20.1	0
μ_m	20.5	21.8
σ_m	0.37	0.35

Table I.1: Weighings of the substrates without the wax layer (S_r) and with the deposited wax layer (S_w). (**Left**) Measurements for substrate N80. (**Right**) measurements for substrate N120.

	N80	**N120**
Wax per sample (mg)	2.06	1.3
Wax per area (mg/mm^2)	0.0119	0.007
Wax per cantilever (mg)	0.0598	0.0377

Table I.2: Wax study results for N80 and N120 samples.

From table figure I.2, it can be observed that the printer responsible for wax deposition exhibits significant variability, as there is 38.09% more wax in WN80 compared to WN120. This introduces another factor that explains the difference in the mechanical properties of these two devices.

I.2 Retardant Effect

To explore the potential production of electrodes using LIG, the effect of fire retardant treatment (trisodium borate, $NaBr_3$) on the produced cantilevers was studied. The effect was analyzed on two distinct substrates: Fire retardant treated Navigator paper 80 g.m^{-2} substrate (FRN80) and Fire retardant treated Whatman chromatography paper grade 1 substrate (FRCP).

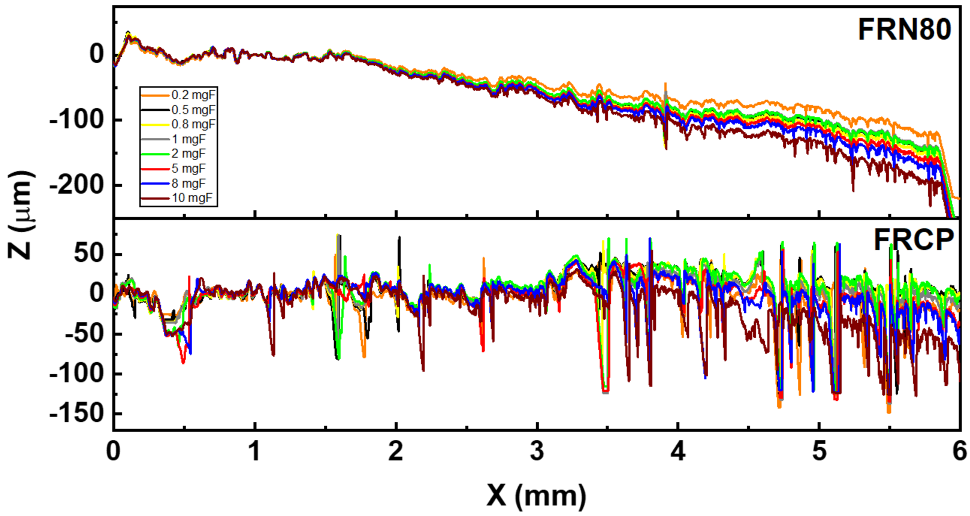

Figure I.1: Cantilever scanning profile, Z axis position with stylus displacement ($Z-X$). **(Top)** FRN80 C1 cantilever, **(bottom)** FRCP C1 cantilever.

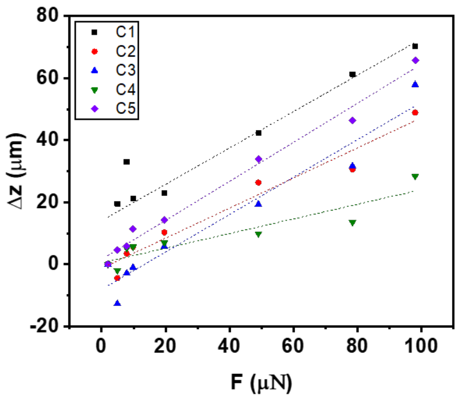

Figure I.2: FRN80 graphical analysis, deflection variation with applied force ($\Delta z - F$) of FRN80 1x5 mm cantilever. Dash lines represent the linear regression for each set of data.

Table I.3: FRN80 cantilevers mechanical characterization.

	m (m.N^{-1})	k_c (N.m^{-1})	E (GPa)
C_1	0.59 ±0.09	1.71	3.41
C_2	0.48±0.04	2.06	4.12
C_3	0.60±0.06	1.66	3.32
C_4	0.24±0.04	4.24	8.48
C_5	0.63±0.03	1.59	3.18
μ_C	0.51	2.25	4.50

Regarding the N80 cantilevers with fire retardant bath, the graph figure I.1 represents a characteristic bending curve of the material. The plots figure I.2 pertain to the deflection as a function of applied force. From the table I.3 average results, the elastic constant of FRN80 cantilevers is 2.25 $N.m^{-1}$ and the Young's modulus is 4.5 GPa. Furthermore, there was a variation in devices associated with the production process, resulting in the fabrication of cantilevers with an elastic constant ranging from 1.44 to 5 $N.m^{-1}$.

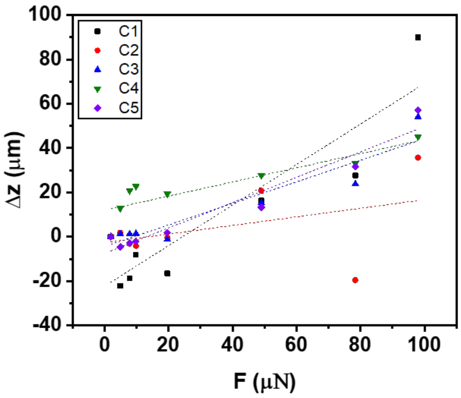

Figure I.3: FRCP graphical analysis, deflection variation with applied force ($\Delta z - F$) of FRCP 1x5 mm cantilever. Dash lines represent the linear regression for each set of data.

Table I.4: FRCP cantilevers mechanical characterization.

	m ($m.N^{-1}$)	k_c ($N.m^{-1}$)	E (GPa)
C_1	0.9 ±0.2	1.09	0.13
C_2	0.19±0.2	5.16	0.59
C_3	0.49±0.07	2.06	0.24
C_4	0.32±0.07	3.13	0.36
C_5	0.57±	1.75	0.20
μ_C	0.50	2.64	0.30

Regarding the CP cantilevers with fire retardant bath, the graph figure I.1 represents a characteristic bending curve of the material. The plots figure I.3 depict the deflection as a function of applied force. From the table I.4 average results, the elastic constant of FRCP cantilevers is 2.64 $N.m^{-1}$ and the Young's modulus is 0.3 GPa. Additionally, a variation in devices was recorded due to the production process, leading to the manufacture of cantilevers with an elastic constant ranging from 0.9 to 1.78 $N.m^{-1}$.

It was expected that CP, due to its higher porosity, would experience a more effective chemical bath and tend to form larger aggregates of this salt within its structure. As the results indicate, there are two distinct trends for each substrate. In the case of N80, the $NaBr_3$ chemical bath induced a considerable increase in elasticity, around 50%. For CP, the results deviate from the trend of N80, which could be attributed to the high uncertainty in measurement associated with this extremely rough substrate.

I.3 Cut Orientation Effect

Towards the end of the laboratory work, the question of preferred orientation of cellulose fibers in a commercial paper sheet arose, leading to the study of this effect on the produced cantilevers. Up to this point, all cantilevers had been produced with the same cutting orientation due to the consistent placement of the paper substrate (horizontal orientation) on the laser cutting stage. By rotating an N80 paper substrate by 90 degrees (figure I.4), the following results were obtained.

Regarding 90ºC rotated Navigator paper 80 $g.m^{-2}$ substrate (RN80), the graph figure I.5 represents a characteristic bending curve of the material. The plots figure I.6 pertain to

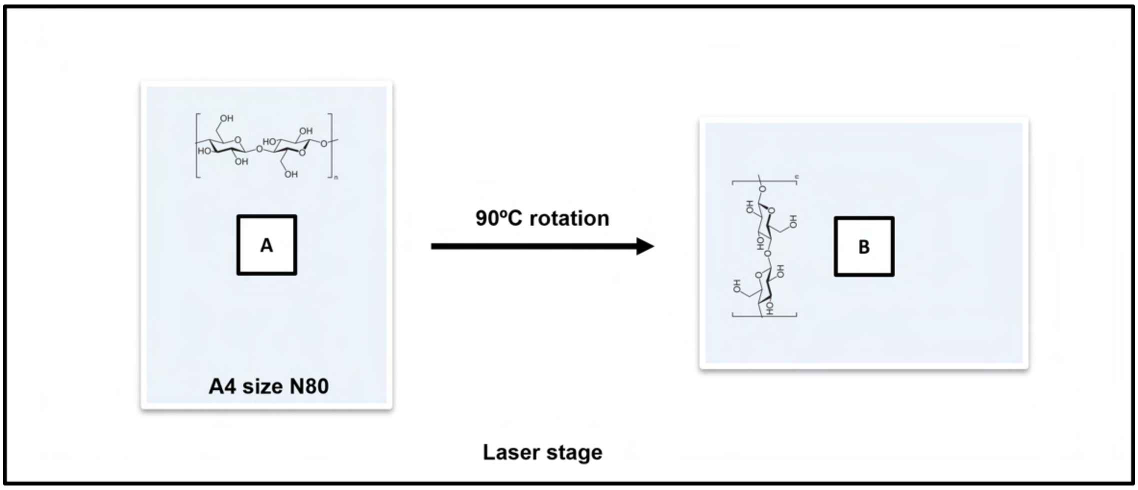

Figure I.4: Schematic representation of the substrates placement.

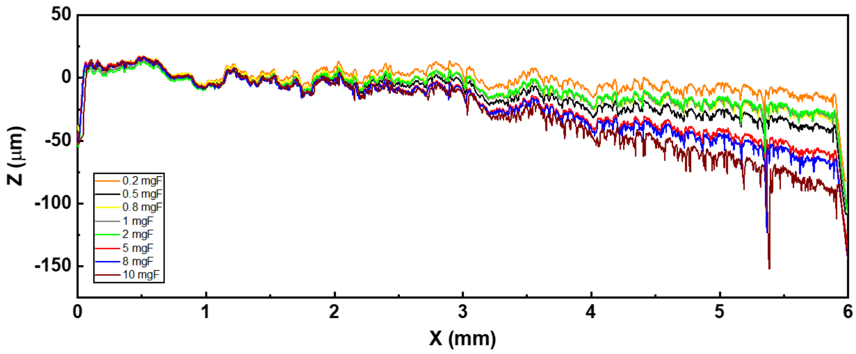

Figure I.5: Scanning profile of RN80 cantilever.

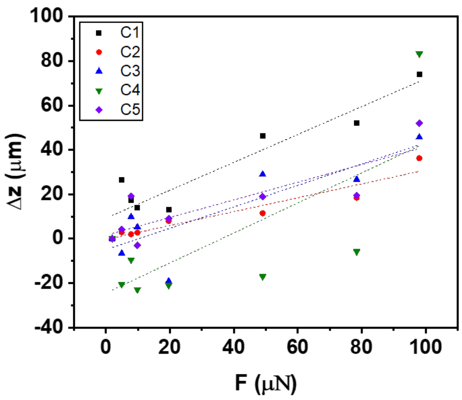

Figure I.6: RN80 graphical analysis, deflection variation with applied force ($\Delta z - F$) of RN80 1 x5mm cantilever. Dash lines represent the linear regression for each set of data.

Table I.5: RN80 cantilevers mechanical characterization.

	m (m.N^{-1})	k$_c$ (N.m^{-1})	E (GPa)
C$_1$	0.63 ±0.09	1.59	3.19
C$_2$	0.31±0.04	3.20	6.40
C$_3$	0.4±0.1	2.07	4.14
C$_4$	0.7±0.3	1.48	2.96
C$_5$	0.40±	2.51	5.03
μ_C	0.50	2.17	4.34

the deflection as a function of applied force. From the table I.5 average results, the elastic constant of WN120 cantilevers is 2.17 $N.m^{-1}$ and the Young's modulus is 4.34 GPa. Once more, there was a variance in devices linked to the production process, resulting in the creation of cantilevers with an elastic constant ranging between 1 to 3.44 $N.m^{-1}$.

The anisotropy of N80 is evident. The significant increase in elasticity of 31.97% highlights the importance of this factor in the final devices, and cutting position do optimizes the deflection of the devices.

This effect was then studied on a previously considered more isotropic cellulose substrate, CP.

The tensile test results are also clear, the Young's modulus of the rotated substrate was 0.13 GPa, this means an increase of 46.15%. As it happens with N80, the CP also have a preferential cutting position to optimize the cantilevers deflection.

II

Complementary Data

II.1 Extended Cantilever Physical Principle and Mathematical Considerations

The expressions describing the cantilever deflection were derived as follows. Figure II.1 illustrates the mathematically described behavior, and all constants are presented in table II.1. The variable M corresponds to the bending constant, and R represents the radius of deflection, which, in turn, is associated with the angle, θ, of deflection.

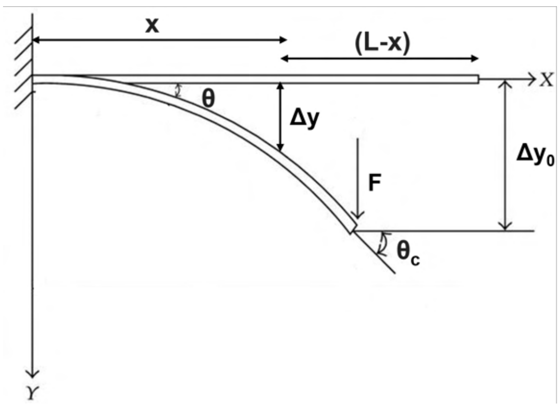

Figure II.1: Sketch depicting the mechanical behavior of the cantilever when a force is applied.

$$M = F \cdot \perp x$$

$$\frac{E}{R} \cdot I = F(L - x)$$

$$\frac{1}{R} = \frac{F}{E \cdot I} \cdot (L - x) = \frac{\partial^2 y}{\partial x^2}$$

$$\Delta_y = \frac{F}{E \cdot I} \left(\frac{Lx^2}{2} - \frac{x^3}{6} \right)$$

Assuming that x is equivalent to the length of the cantilever (L), we are now deducing the deflection at the end of the beam (Δy_0.

$$x = L \rightarrow \Delta y = \Delta y_0$$

$$\Delta y_0 = \frac{F}{E \cdot I} \cdot \frac{L}{3}$$

$$F = \frac{3E \cdot I}{L^3} \cdot \Delta y_0$$

The moment of inertia, I, for a rectangular-shaped cantilever can be described by the following formula.

$$I = \frac{w \cdot t^3}{12}$$

Finally, I managed to attain the parameters describing the cantilever and its materials, k_c and E.

$$F = \frac{E \cdot W \cdot t^3}{4L^3} \cdot \Delta y$$

$$F = k_c \cdot \Delta y$$

$$E = \frac{k_c 4L^3}{t^3 W}$$

Table II.1: Comparative analysis of parameters in tensile and bending tests.

	Tensile Test	**Bending Test**
Force	$k_c \Delta x$	$k_c \Delta y$
Elastic Constant	$\frac{EA}{l_0}$	$\frac{Et^3 W}{4L^3}$
Young's Modulus	$\frac{k_c l_0}{A}$	$\frac{k_c 4L^3}{t^3 W}$

II.2 Commercial Paper Substrates

The commercial paper used in this work, N80 and N120, is produced from *Eucalyptus Globulus* wood pulp by the Navigator Company and has the following characteristics, according to the manufacturer (table II.2).

Table II.2: Schematic for the physical behaviour of cantilever under an applied force.

Grammage (g.m^{-2})	**80**	**120**
Thickness (μm))	110	128
CIE Whiteness	169	169
Roughness (mL.min^{-1}	120	50
Opacity (%)	95	98

The CP paper was also used, which has the following properties, as stated by Whatman (table II.3).

Table II.3: The specifications for the CP produced by Whatman.

Grade	**1**
Description	medium flow
Particle Retention Liquid (μm)	11
Filtration Speed Herzberg (s)	150
Air Flow (mL.mm^{-2})	6774
Thickness (μm))	180
Basis Weight (g.m^{-2})	88

II.3 Nanofibrillated Cellulose Coating Details

The commercial printing paper was laminated with a nanofibrillated cellulose membrane (CMN80, CMN120). The following materials were used: nanofibrillated gel with 2% of solid content, deionized water, N80, N120, Petri dish, and desiccator. In order to prepare a aqueous suspension of Nanofibrillated Cellulose (NFC), 11.5 g of nanofibrillated gel with 2% of solid content, was weighed in a 100 mL beaker, and 35 mL of deionized water was added to prepare the aqueous suspension. A small magnet was introduced into the solution, which was then placed on a magnetic stirrer and agitated (200 RPM for 15 min). Meanwhile, the acrylic petri dishes (measuring L = 11.7 cm, W = 11.7 cm), where the membranes would be produced, were cleaned with deionized water, and substrates N80 and N120 were cut to match the dimensions and shape of the petri dishes. After the 0.25 h of agitation, the solution became homogeneous and was poured onto the petri dishes, covering their entire surface area. The petri dishes were then placed in an oven at 40 ºC for 15h. By the end of this time, the solution would have gained some consistency, ready to receive the previously cut substrates, and a new 15 h cycle in the oven at 40 ºC is initiated. During this process, it is essential to periodically remove condensation droplets that may form inside the desiccator, while visually inspecting the formation and drying process of the membrane. It is noteworthy that the drying time is not linear, so the frequency of visual inspections should increase as the desiccator cycle nears completion.

II.4 LIG on Paper Details

In order to induce the formation of graphene for the electrodes and conductive tracks, a 0.1 M solution of sodium tetraborate fire retardant was prepared. Subsequently, a chemical bath of CP paper was carried out in the previously prepared solution for 20 minutes (with the paper's face flipped at 10 minutes). After the chemical bath, the substrates were subjected to a thermal treatment in an oven at 40 °C for 16h. Following the substrate preparation, they were positioned on the laser stage and subjected to a matrix power variation with the equipment's speed of a rectangular test pattern designed in Adobe Illustrator software. Finally, the resistance of the test squares was measured using a commercial multimeter.

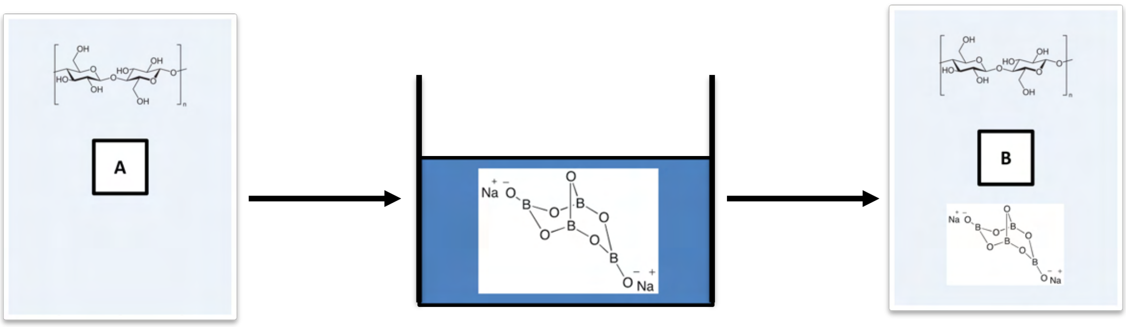

Figure II.2: LIG on paper preparation diagram.

II.5 Cantilevers Bending Tests

The following tables present the average deflections and their respective standard deviations.

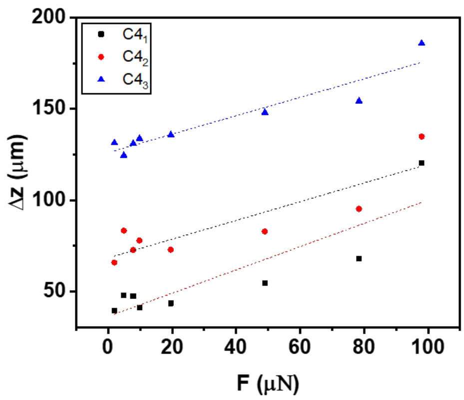

Table II.4: C4 graphical analysis, deflection variation with applied force ($\Delta z - F$) of C4 1x4 mm cantilever. Dash lines represent the linear regression for each set of data.

Table II.5: C4 cantilevers mechanical characterization.

	m (m.N^{-1})	k$_c$ (N.m^{-1})	E (GPa)
C$_1$	0.6 ± 0.1	1.56	1.60
C$_2$	0.5 ± 0.1	1.96	2.01
C$_3$	0.50 ± 0.07	2.00	2.05
μ_C	0.53	1.8	1.9
σ_C	0.06	0.2	0.2

II.6 Supplementary Figures

Here is the photographic documentation mentioned in the chapter 3.

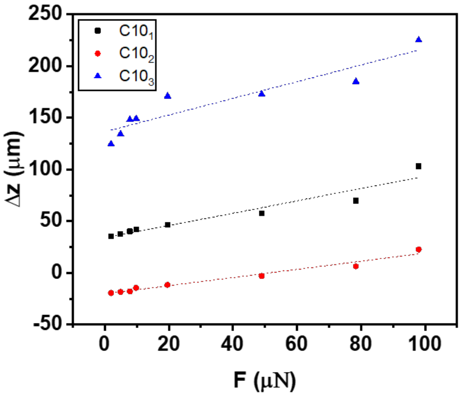

Table II.6: C10 graphical analysis, deflection variation with applied force ($\Delta z - F$) of C10 1x10 mm cantilever. Dash lines represent the linear regression for each set of data.

Table II.7: C10 cantilevers mechanical characterization.

	m (m.N^{-1})	k$_c$ (N.m^{-1})	E (GPa)
C$_1$	0.59 ± 0.07	1.69	1.74
C$_2$	0.39 ± 0.02	2.78	2.84
C$_3$	0.8 ± 0.1	1.25	1.28
μ_C	0.6	1.9	2.0
σ_C	0.2	0.8	0.8

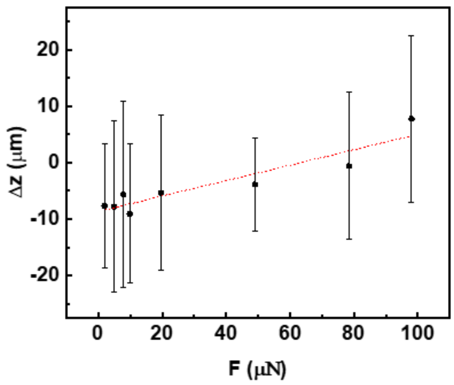

Figure II.3: PEN graphical analysis, deflection variation with applied force ($\Delta z - F$) of PEN 1x5 mm cantilever. Dash line represents the linear regression for the average deflection PEN cantilever.

Table II.8: PEN cantilevers mechanical characterization.

F (μN)	$\mu_{\Delta z}$ (μm)	$\sigma_{\Delta z}$ (μm)
1.96	-7.67	11.10
4.90	-7.81	15.21
7.84	-5.68	16.50
9.80	-9.05	12.34
19.60	-5.33	13.83
49.00	-3.88	8.20
78.40	-0.62	13.05
98.00	7.77	14.79

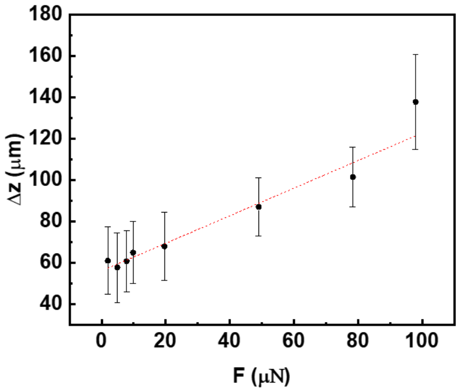

Figure II.4: N80 graphical analysis, deflection variation with applied force ($\Delta z - F$) of N80 1x5 mm cantilever. Dash line represents the linear regression for the average deflection N80 cantilever.

Table II.9: N80 cantilevers mechanical characterization.

F (μN)	$\mu_{\Delta z}$ (μm)	$\sigma_{\Delta z}$ (μm)
1.96	61.09	16.21
4.90	57.73	16.80
7.84	60.77	14.95
9.80	65.00	15.14
19.60	68.01	16.44
49.00	87.10	14.21
78.40	101.59	14.40
98.00	137.90	23.05

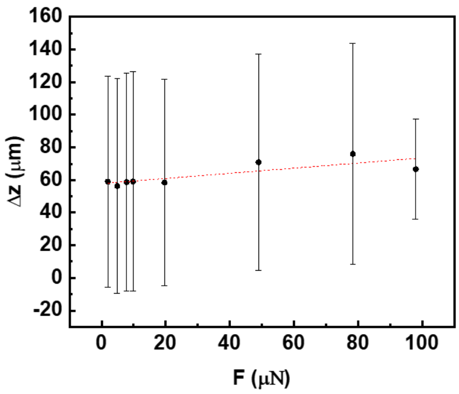

Figure II.5: N120 graphical analysis, deflection variation with applied force ($\Delta z - F$) of N120 1x5 mm cantilever. Dash line represents the linear regression for the average deflection N120 cantilever.

Table II.10: N120 cantilevers mechanical characterization.

F (μN)	$\mu_{\Delta z}$ (μm)	$\sigma_{\Delta z}$ (μm)
1.96	59.01	64.67
4.90	56.34	65.75
7.84	58.67	66.78
9.80	59.09	67.21
19.60	58.46	63.44
49.00	70.93	66.20
78.40	75.98	67.82
98.00	66.62	30.60

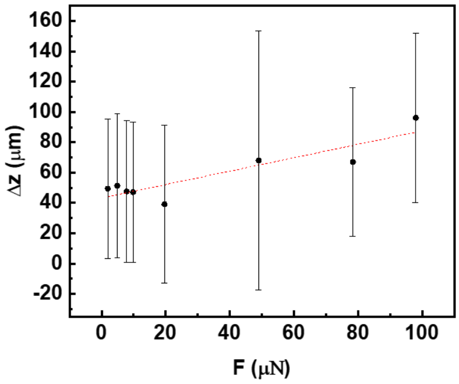

Figure II.6: CP graphical analysis, deflection variation with applied force ($\Delta z - F$) of CP 1x5 mm cantilever. Dash line represents the linear regression for the average deflection CP cantilever.

Table II.11: CP cantilevers mechanical characterization.

F (μN)	$\mu_{\Delta z}$ **(μm)**	$\sigma_{\Delta z}$ **(μm)**
1.96	49.40	45.82
4.90	51.41	47.35
7.84	47.61	46.95
9.80	47.08	46.45
19.60	39.22	51.96
49.00	68.03	85.61
78.40	66.97	49.06
98.00	96.24	55.98

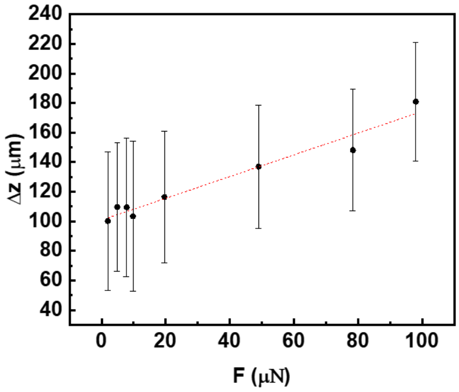

Figure II.7: WN80 graphical analysis, deflection variation with applied force ($\Delta z - F$) of WN80 1x5 mm cantilever. Dash line represents the linear regression for the average deflection WN80 cantilever.

Table II.12: WN80 cantilevers mechanical characterization.

F (μN)	$\mu_{\Delta z}$ **(μm)**	$\sigma_{\Delta z}$ **(μm)**
1.96	100.19	46.98
4.90	109.61	43.45
7.84	109.46	46.90
9.80	103.41	50.58
19.60	116.40	44.31
49.00	137.01	41.63
78.40	148.15	41.15
98.00	181.01	40.16

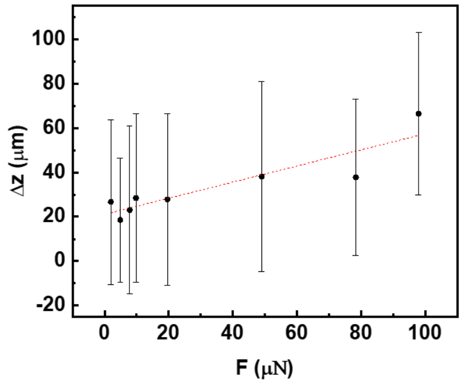

Figure II.8: WN120 graphical analysis, deflection variation with applied force ($\Delta z - F$) of WN120 1x5 mm cantilever. Dash line represents the linear regression for the average deflection WN120 cantilever.

Table II.13: WN120 cantilevers mechanical characterization.

F (μN)	$\mu_{\Delta z}$ **(μm)**	$\sigma_{\Delta z}$ **(μm)**
1.96	26.73	37.13
4.90	18.57	27.97
7.84	23.07	37.91
9.80	28.45	38.04
19.60	27.83	38.71
49.00	38.08	42.78
78.40	37.80	35.26
98.00	66.41	36.54

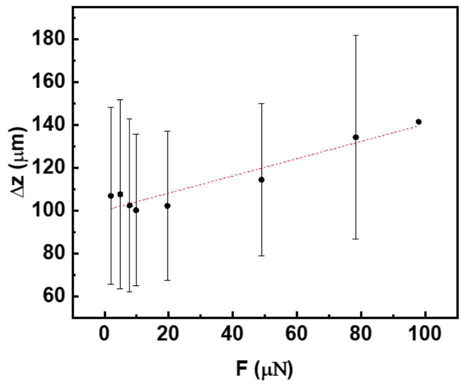

Figure II.9: CMN80 graphical analysis, deflection variation with applied force ($\Delta z - F$) of CMN80 1x5 mm cantilever. Dash line represents the linear regression for the average deflection CMN80 cantilever.

Table II.14: CMN80 cantilevers mechanical characterization.

F (μN)	$\mu_{\Delta z}$ **(μm)**	$\sigma_{\Delta z}$ **(μm)**
1.96	106.99	41.34
4.90	107.69	44.09
7.84	102.49	40.44
9.80	100.25	35.36
19.60	102.30	34.79
49.00	114.49	35.74
78.40	134.29	47.47
98.00	141.56	*

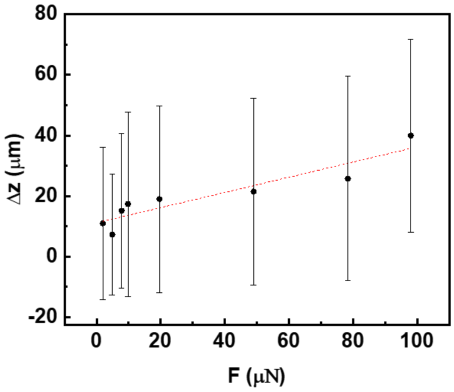

Figure II.10: CMN120 graphical analysis, deflection variation with applied force ($\Delta z - F$) of CMN120 1x5 mm cantilever. Dash line represents the linear regression for the average deflection CMN120 cantilever.

Table II.15: CMN120 cantilevers mechanical characterization.

F (μN)	$\mu_{\Delta z}$ **(μm)**	$\sigma_{\Delta z}$ **(μm)**
1.96	11.01	25.13
4.90	7.24	19.90
7.84	15.16	25.57
9.80	17.38	30.46
19.60	19.01	30.88
49.00	21.50	30.87
78.40	25.78	33.76
98.00	39.98	31.84

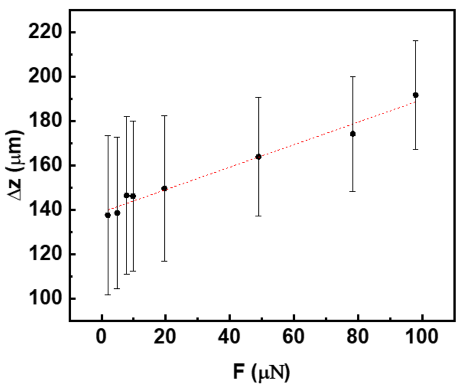

Figure II.11: FRN80 graphical analysis, deflection variation with applied force ($\Delta z - F$) of FRN80 1x5 mm cantilever. Dash line represents the linear regression for the average deflection FRN80 cantilever.

Table II.16: FRN80 cantilevers mechanical characterization.

F (μN)	$\mu_{\Delta z}$ **(μm)**	$\sigma_{\Delta z}$ **(μm)**
1.96	137.62	35.84
4.90	138.64	34.24
7.84	146.56	35.73
9.80	146.22	33.69
19.60	149.67	32.76
49.00	163.97	26.70
78.40	174.32	25.93
98.00	191.84	24.46

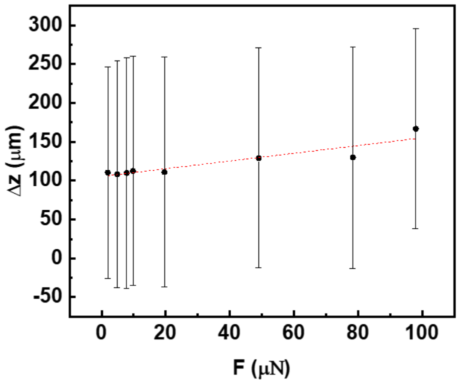

Figure II.12: FRCP graphical analysis, deflection variation with applied force ($\Delta z - F$) of FRCP 1x5 mm cantilever. Dash line represents the linear regression for the average deflection FRCP cantilever.

Table II.17: FRCP cantilevers mechanical characterization.

F (μN)	$\mu_{\Delta z}$ (μm)	$\sigma_{\Delta z}$ (μm)
1.96	110.49	136.42
4.90	108.34	145.72
7.84	110.01	148.61
9.80	112.50	147.51
19.60	111.12	147.76
49.00	129.19	141.44
78.40	129.80	142.63
98.00	166.86	128.48

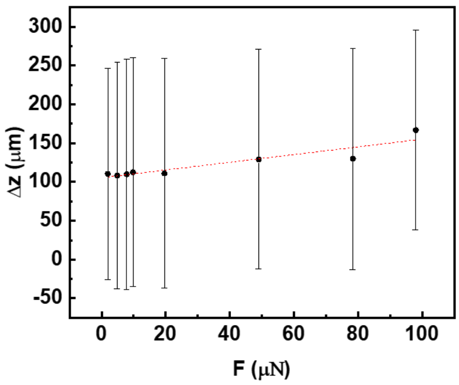

Figure II.13: RN80 graphical analysis, deflection variation with applied force ($\Delta z - F$) of RN80 1x5 mm cantilever. Dash line represents the linear regression for the average deflection RN80 cantilever.

Table II.18: RN80 cantilevers mechanical characterization.

F (μN)	$\mu_{\Delta z}$ (μm)	$\sigma_{\Delta z}$ (μm)
1.96	53.78	35.26
4.90	55.11	24.11
7.84	61.55	33.41
9.80	53.00	29.88
19.60	51.75	21.84
49.00	71.51	33.05
78.40	75.92	29.41
98.00	112.00	42.82

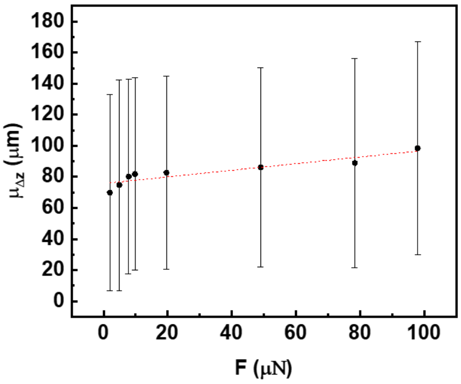

Figure II.14: POC graphical analysis, deflection variation with applied force ($\Delta z - F$) of POC 2x5 mm cantilever. Dash line represents the linear regression for the average deflection POC cantilever.

Table II.19: POC cantilevers mechanical characterization.

F (μN)	**$\mu_{\Delta z}$ (μm)**	**$\sigma_{\Delta z}$ (μm)**
1.96	69.87	63.23
4.90	74.65	67.73
7.84	80.15	62.60
9.80	81.76	61.90
19.60	82.69	62.20
49.00	86.10	64.36
78.40	88.88	67.36
98.00	98.44	68.74

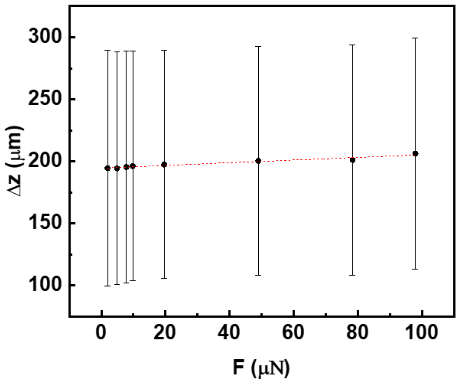

Figure II.15: ePOC graphical analysis, deflection variation with applied force ($\Delta z - F$) of ePOC 2x5 mm cantilever. Dash line represents the linear regression for the average deflection ePOC cantilever.

Table II.20: ePOC cantilevers mechanical characterization.

F (μN)	**$\mu_{\Delta z}$ (μm)**	**$\sigma_{\Delta z}$ (μm)**
1.96	194.49	94.79
4.90	194.29	93.71
7.84	195.43	93.39
9.80	196.15	92.44
19.60	197.51	91.97
49.00	200.36	92.41
78.40	201.07	92.89
98.00	206.29	93.05

Table II.21: N80 cantilevers mechanical characterization.

	m (m.N^{-1})	**k_c (N.m^{-1})**	**E (GPa)**
C_1	0.59 ± 0.09	1.71	3.41
C_2	0.48± 0.04	2.06	4.12
C_3	0.6± 0.06	1.66	3.32
C_4	0.24± 0.04	4.24	8.48
C_5	0.63± 0.03	1.59	3.18
μ_C	0.5	2	5
σ_C	0.2	1	2

Table II.22: N120 cantilevers mechanical characterization.

	m (m.N^{-1})	**k_c (N.m^{-1})**	**E (GPa)**
C_1	0.4 ± 0.1	2.42	1.70
C_2	0.21± 0.06	4.86	3.40
C_3	0.23± 0.05	4.34	3.04
C_4	0.27± 0.05	3.64	2.55
C_5	0.41± 0.04	2.41	1.69
μ_C	0.3	3	2.5
σ_C	0.1	1	0.8

Table II.23: PEN cantilevers mechanical characterization.

	m (m.N^{-1})	k$_c$ (N.m^{-1})	E (GPa)
C_1	0.1 ± 0.02	13.67	12.48
C_2	0.12± 0.08	8.4	7.68
C_3	0.19± 0.05	5.19	4.74
C_4	0.10± 0.02	9.73	8.89
C_5	0.20± 0.03	5.09	4.65
μ_C	0.14	8	8
σ_C	0.06	3	3

Table II.24: CP cantilevers mechanical characterization.

	m (m.N^{-1})	k$_c$ (N.m^{-1})	E (GPa)
C_1	0.70 ± 0.07	1.43	0.17
C_2	0.4± 0.2	2.72	0.31
C_3	0.5± 0.3	2.12	0.24
C_4	0.5± 0.1	1.99	0.23
C_5	0.17± 0.08	5.65	0.65
μ_C	0.4	3	0.3
σ_C	0.2	2	0.2

Table II.25: WN80 cantilevers mechanical characterization.

	m (m.N^{-1})	k$_c$ (N.m^{-1})	E (GPa)
C_1	0.77 ±0.08	1.29	0.51
C_2	0.9±0.1	1.11	0.44
C_3	0.58±0.08	1.73	0.68
C_4	0.71±0.08	1.41	0.56
C_5	0.56±0.05	1.77	0.70
μ_C	0.7	1.5	0.6
σ_C	0.1	0.3	0.1

Table II.26: WN120 cantilevers mechanical characterization.

	m (m.N^{-1})	k$_c$ (N.m^{-1})	E (GPa)
C_1	0.52±0.05	1.90	0.32
C_2	0.40±0.09	2.47	0.42
C_3	*	*	*
C_4	0.31±0.03	3.19	0.54
C_5	0.26±	3.76	0.64
μ_C	0.4	2.8	0.5
σ_C	0.1	0.8	0.1

Table II.27: CMN80 cantilevers mechanical characterization.

	m (m.N^{-1})	k$_c$ (N.m^{-1})	E (GPa)
C_1	-0.3 ±0.3	*	*
C_2	0.67±0.05	1.48	1.86
C_3	0.83±0.07	1.20	1.50
C_4	0.35±0.06	2.86	3.59
C_5	0.6±0.1	1.68	2.11
μ_C	0.6	1.8	2.3
σ_C	0.2	0.7	0.9

Table II.28: CMN120 cantilevers mechanical characterization. C_1 was considered as an outlier and it was excluded from the statistical analysis.

	m (m.N^{-1})	k$_c$ (N.m^{-1})	E (GPa)
C_1	0.05 ±0.02	18.25	6.82
C_2	0.09±0.01	10.93	4.08
C_3	0.3±0.1	3.02	1.13
C_4	0.22±0.7	4.58	1.71
C_5	0.12±	8.67	3.24
μ_C	0.2	7	3
σ_C	0.1	4	1

Table II.29: POC cantilevers mechanical characterization.

	m (m.N^{-1})	k$_c$ (N.m^{-1})	E (GPa)
C_1	0.13 ±0.07	7.94	4.98
C_2	0.16±0.06	6.08	3.81
C_3	0.29±0.04	3.42	2.15
C_4	0.28±0.03	3.63	2.28
C_5	*	*	*
μ_C	0.21	5	3
σ_C	2	2	1

Table II.30: ePOC cantilevers mechanical characterization. C_3 was considered as an outlier and it was excluded from the statistical analysis.

	m (m.N^{-1})	k$_c$ (N.m^{-1})	E (GPa)
C_1	0.08 ±0.02	11.89	7.45
C_2	0.07±0.02	15.30	9.59
C_3	0.02±0.02	58.65	36.78
C_4	0.16±0.02	6.14	3.85
C_5	0.21±0.03	4.74	2.97
μ_C	0.13	9	6
σ_C	0.07	5	3

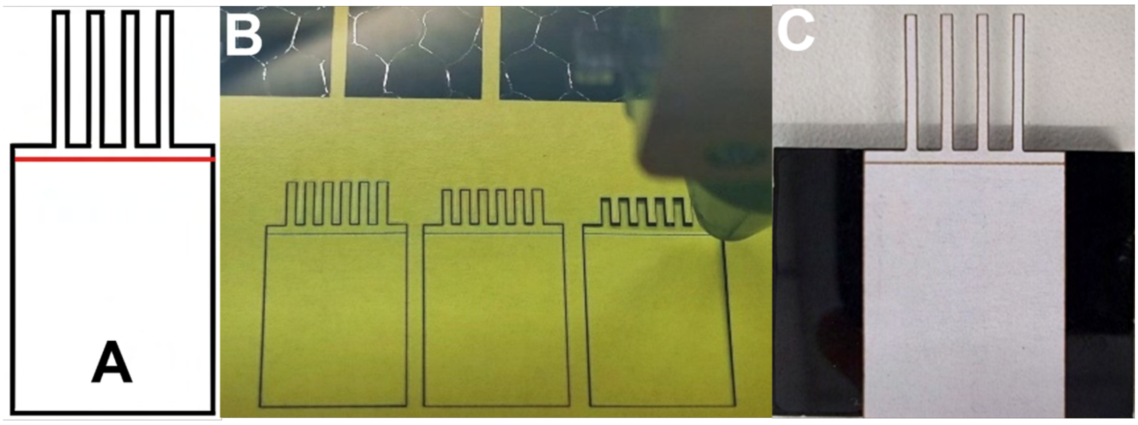

Figure II.16: Cantilever photographic record, production process and setup. (**A**) Adobe Illustrator layout, (**B**) Photo of the laser beam cutting a WN80 sample, (**C**) Set of four 1x10mm cantilevers already attached to the acrylic chip.

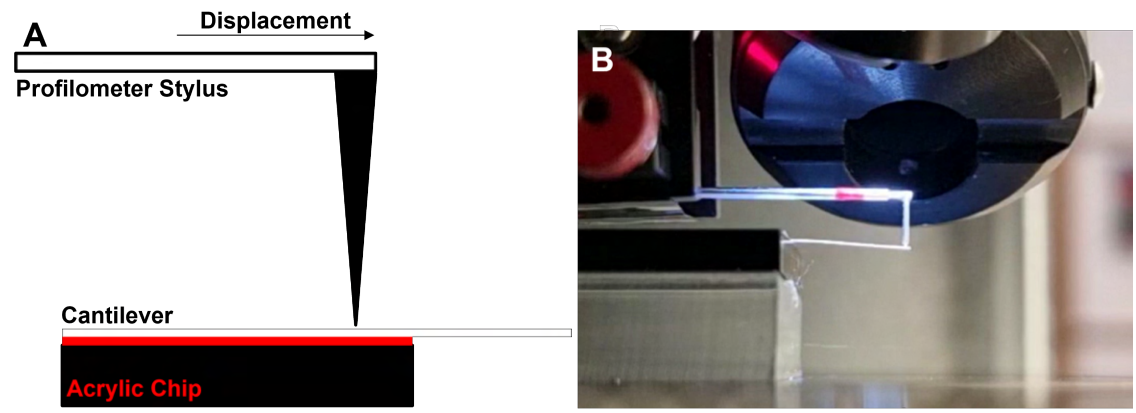

Figure II.17: Contact profilometry technique photographic record. (**A**) XP-Plus Stylus Profiler, (**A**) Contact profilometry diagram, (**B**) Photo of the scanning process, deflection is visible.

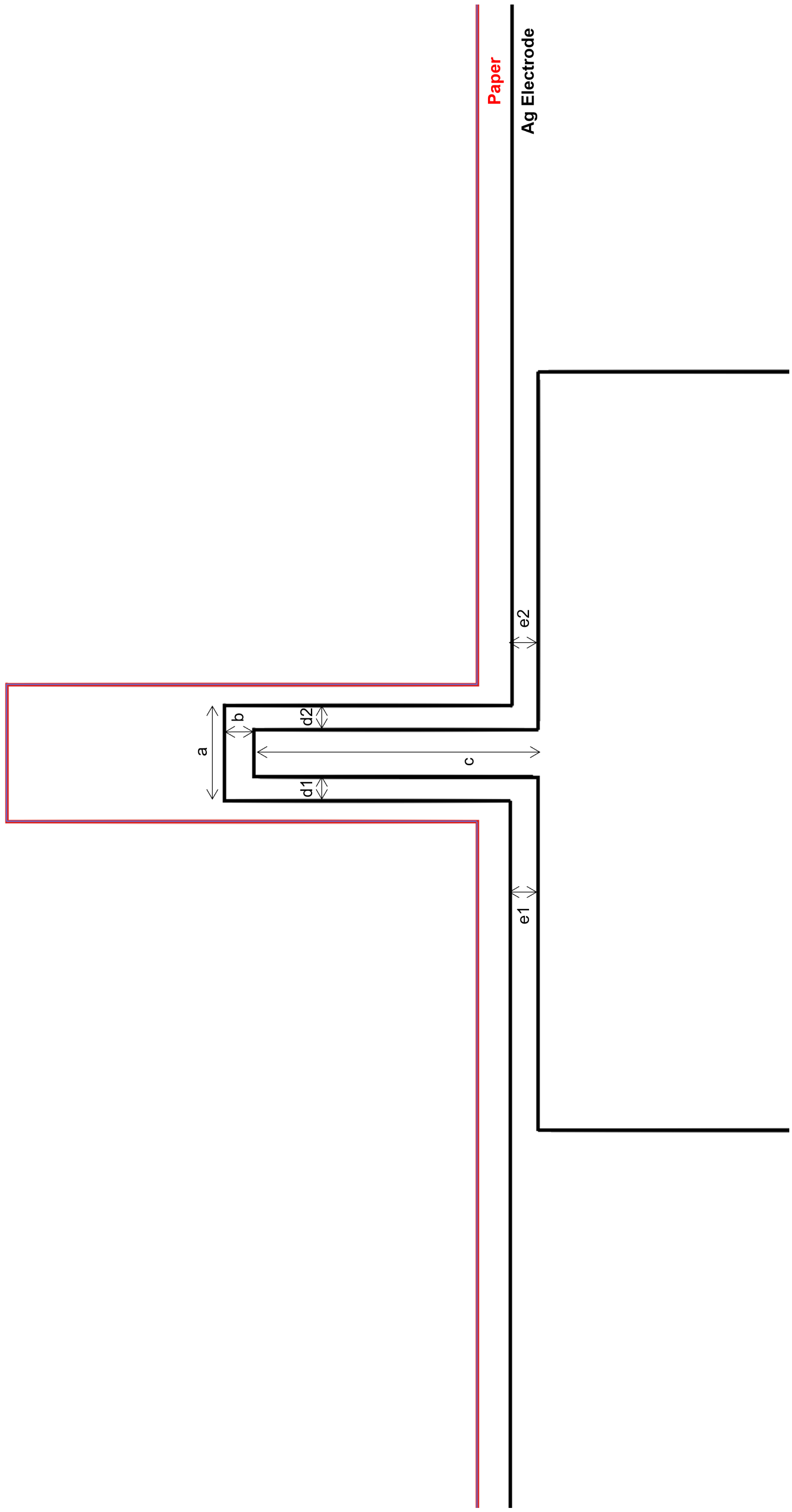

Figure II.18: Figure with the reference dimensions considered to characterize table 4.11.